

The SuperCOSMOS Sky Survey. Paper II: Image detection, parameterisation, classification and photometry

N.C. Hambly¹, M.J. Irwin² and H.T. MacGillivray¹

¹Wide Field Astronomy Unit, Institute for Astronomy, University of Edinburgh, Blackford Hill, Edinburgh, EH9 3HJ

²Cambridge Astronomy Survey Unit, Institute for Astronomy, Madingley Road, Cambridge, CB3 0HA

Accepted —. Received —; in original form —

ABSTRACT

In this, the second in a series of three papers concerning the SuperCOSMOS Sky Survey, we describe the methods for image detection, parameterisation, classification and photometry. We demonstrate the internal and external accuracy of our object parameters. Using examples from the first release of data, the South Galactic Cap survey, we show that our image detection completeness is close to 100% to within ~ 1.5 mag of the nominal plate limits. We show that for the B_J survey data, the image classification is *externally* $> 99\%$ reliable to $B_J \sim 19.5$. Internally, the image classification is reliable at a level of $> 90\%$ to $B_J \sim 21$, $R \sim 19$. The photometric accuracy of our data is typically ~ 0.3 mag with respect to external data for $m > 15$. Internally, the relative photometric accuracy in restricted position and magnitude ranges can be as accurate as $\sim 5\%$ for well exposed stellar images. Colours are externally accurate to $\sigma_{B-R,R-I} \sim 0.07$ at $B_J \sim 16.5$ rising to $\sigma_{B-R,R-I} \sim 0.16$ at $B_J \sim 20$.

Key words: astronomical databases: miscellaneous – catalogues – surveys – methods: data analysis – techniques: image processing, photometric

1 INTRODUCTION

In Paper I of this series (Hambly et al. 2001a) we describe the SuperCOSMOS Sky Survey programme (hereafter SSS). This project is to scan the multi-colour/multi-epoch Schmidt photographic atlas material to produce a digitised survey of the sky in three colours (BRI), one colour (R) at two epochs. The ultimate aim of the project is to cover the entire sky; the first release of data from the programme was the South Galactic Cap (hereafter SGC) survey. The SGC survey covers ~ 5000 square degrees of the southern sky at Galactic latitudes $|b| > 60^\circ$. Paper III in this series describes the derivation of the astrometric parameters for the SSS (Hambly et al. 2001b). In this, the second paper of the series, we describe in some detail the image detection, parameterisation and classification procedures for the programme. We also describe the techniques for photometric calibration.

Paper I is intended as a User Guide for the survey data. It describes the database organisation and demonstrates specific examples of the use of the data. Papers II and III provide technical details concerning the derivation of object catalogue parameters available from the survey database, and also demonstrate the precision of these with

respect to external data from other sources. In these papers, we demonstrate examples and make comparisons using data from the SGC survey. All the results, however, are generally applicable to the SSS data as a whole at Galactic latitudes $|b| \geq 30^\circ$. At lower latitudes, image crowding will of course degrade astrometric and photometric performance.

The plate material used in the SSS is detailed in Paper I, and consists of sky-limited Schmidt photographic glass plate and film originals, or glass copies of glass originals, taken with the UK, ESO and Palomar Oschin Schmidt Telescopes (for more details see Morgan et al. 1992 and references therein). Hereafter, the SERC–J/EJ survey will be referred to simply as the J survey; the AAO–R/SERC–ER as the R survey and the SERC–I as the I survey.

2 METHODOLOGY

2.1 Pixel analysis

2.1.1 Digitisation

The SuperCOSMOS machine digitises the scanned photograph at $10\mu\text{m}$ resolution (0.67 arcsec) in 15-bit grey levels (further details of the hardware are given in Hambly et

arXiv:astro-ph/0108290v1 17 Aug 2001

al. 1998). Pixel values are in transmission units and are related to incident intensity via the usual transmission (T), density (D) and intensity (I) relationships on the the log-linear part of the photographic characteristic curve:

$$\gamma \log_{10} I \propto D \propto \log_{10}(1/T), \quad (1)$$

where γ is the gradient of the response in the $D - \log_{10} I$ plane. Each photograph is digitised in ~ 2 hr, producing ~ 2 Gbyte of data. The pixel map is ‘blocked down’ in 64×64 pixel cells during scanning to produce a raw median sky map; all subsequent processing is then carried out offline.

2.1.2 Sky estimation

Object detection in the raw pixel map requires an estimate of the sky value at every point within the two-dimensional image. The raw median values of the sky are first filtered using a weighted median filter (Brownrigg 1984) of the form

$$\begin{array}{ccc} 1 & 1 & 1 \\ 1 & 3 & 1 \\ 1 & 1 & 1 \end{array}$$

applied over filtering scales of 3, 2 and 1 blocks (e.g. Stobie 1986). This results in variations in scale size greater than ~ 2 mm (or ~ 2 arcmin) being retained as sky variations in the background array. This is obviously a compromise between detection of low surface brightness objects at this scale or greater and accurate image parameterisation in areas of real sky variation. Experiments with differing scale lengths showed that the choice of raw blocking of 0.64 mm squares coupled with iterative filtering scale sizes of 3, 2 and 1 (e.g. Stobie 1986) is optimal in terms of minimising spurious detections due to, for example, low level scattered light around bright stars (see also MacGillivray & Stobie 1984).

2.1.3 Transmission to intensity calibration

Most modern Schmidt photographs have one or more intensity calibration ‘step-wedges’ exposed on their sides or corners (see, for example, Tritton 1983). In principle, it is possible to measure the transmission of the various intensity spots and calibrate measured transmission into incident relative intensity. In practice, however, there are a number of reasons why even rough step-wedge calibration is difficult to achieve. Variations in emulsion sensitivity across the plate and non-uniform illumination of the wedge spots themselves can cause large errors. Also, the fact that SuperCOSMOS scans by illumination of a strip of emulsion means that when imaging dense spots, the light levels recorded are badly affected by diffracted light originating from relatively clear emulsion surrounding the spot. Measurements of the 16-spot KPNO step wedges on modern UKSTU plates using a Macbeth diffuse densitometer show values of characteristic curve gradient $\gamma \sim 2 \pm 10\%$ (indeed, such a value is a criterion for a survey-grade plate and inclusion in the final UKSTU photographic sky atlases). Hence, we use an *assumed* transmission-to-intensity calibration with slope corresponding to $\gamma \approx 2$ (older glass copies of the POSS-I ‘E’ survey are analysed using a different value due to their poorer contrast). This procedure is vindicated not least by the demonstration, in Section 2.3.1, of measurements of the gradients

of the instrumental magnitude scale with respect to CCD data, where we show that the resulting scales have close to unit gradient with scatter at around the 10% level.

2.1.4 Thresholding and image parameterisation

Image detection requires thresholding above a local sky estimate. The SSS pixel data are thresholded at a constant percentage cut above local sky. A sky noise parameter σ_{SKY_0} is determined from a small ($\sim 10 \times 10$ arcmin) region of image data near the centre of each plate. The sky background value I_{SKY_0} in this region is determined as described in Beard, MacGillivray & Thanisch (1990) while the σ_{SKY_0} estimator uses the relationship $\sigma_{\text{SKY}_0} = 1.48 \times \text{MAD}_{\text{SKY}_0}$, where $\text{MAD}_{\text{SKY}_0}$ is the median of absolute deviations of the pixel values about the sky estimate (the factor 1.48 is the scaling needed to convert the MAD estimate for a Gaussian distribution to the equivalent Gaussian sigma). This yields a ‘percentage cut’ value PCUT ($= 100 \times 2.3\sigma_{\text{SKY}_0}/I_{\text{SKY}_0}$) such that at any part of the image

$$I_{\text{THRESH}} = \frac{(100 + \text{PCUT})}{100} \times I_{\text{SKY}}, \quad (2)$$

where I_{THRESH} is the threshold intensity, I_{SKY} is the local sky estimate based on bilinear interpolation of the filtered sky map, and PCUT is typically 7% for survey plates. Note that this single-parameter multiplicative thresholding is designed to cope with the fact that the sky level (and therefore the noise level) changes over the Schmidt field due to vignetting, and a zeropoint sky intensity value is chosen for the transmission-to-intensity calibration such that the threshold, in terms of the number of σ above sky, remains constant regardless of sky variations.

Once the thresholded pixel set has been determined for a plate, pixel connectivity can be analysed and image parameterisation can take place. The details of the COSMOS pixel analyser are contained in MacGillivray & Stobie (1984), Stobie (1986) and Beard et al. (1990) and will not be repeated here; however we describe some details that are relevant to SuperCOSMOS survey data. Many of the techniques used are similar to those developed for the APM machine (e.g. Irwin 1985; Draper & Eaton 1999).

For image detection, 8-fold nearest-neighbour pixel connectivity is used along with a criterion that images must contain at least 8 connected pixels (the so-called ‘area cut’). Rethresholding at 16 levels defined as in Beard et al. (1990) Equation 2, with a ‘deblend parameter’ of $D = 1.05$ detects multiple objects via fragmentation; in addition rethresholding at 8 levels defined by

$$I_{\text{AP}n} = I_{\text{THRESH}} + 2^{n-2} \times \sigma_{\text{SKY}_0}, n = 1, 2, \dots, 8 \quad (3)$$

is used to supply a set of 8 ‘areal profiles’ at intensity levels of 0.5σ , 1σ , 2σ , 4σ ... above the zeroth areal profile level I_{THRESH} . These provide a set of measurements of the areal extent (in pixels) of each image, and can be used for morphological classification (see Section 2.2.3). Note that these areal profile levels are different to those originally used for the COSMOS machine (MacGillivray & Stobie 1984). This new definition provides optimal levels for stellar profile analysis (see later).

Object parameterisation proceeds for each detected object as described in Stobie (1986), with both unit-weighted

No.	Name	Description	Units	Comments
1	RA	Celestial Right Ascension	10^{-8} radians	see Section 2.2.1
2	DEC	Celestial Declination	10^{-8} radians	see Section 2.2.1
3	XMIN	Left extent	0.01 micron	
4	XMAX	Right extent	0.01 micron	
5	YMIN	Bottom extent	0.01 micron	
6	YMAX	Top extent	0.01 micron	
7	AREA	Total area	Pixels	
8	IPEAK	Peak intensity	Intensity	I_{PEAK}
9	COSMAG	Isophotal magnitude	Millimag	Equation 4
10	ISKY	Sky intensity at (XCEN_I, YCEN_I)	Intensity	I_{SKY} , e.g. Equation 2
11	XCEN_I	Intensity weighted X centroid	0.01 micron	
12	YCEN_I	Intensity weighted Y centroid	0.01 micron	
13	A_U	Unweighted semi-major axis	0.01 micron	
14	B_U	Unweighted semi-minor axis	0.01 micron	
15	THETA_U	Unweighted orientation	Degrees	
16	A_I	Weighted semi-major axis	0.01 micron	
17	B_I	Weighted semi-minor axis	0.01 micron	
18	THETA_I	Weighted orientation	Degrees	
19	CLASS	Classification flag		see Section 2.2.3
20	P_A	Celestial position angle	Degrees	see Section 2.2.1
21	AP(1)	Area above areal profile level 1	Pixels	Equation 3
22	AP(2)	Area above areal profile level 2	Pixels	
23	AP(3)	Area above areal profile level 3	Pixels	
24	AP(4)	Area above areal profile level 4	Pixels	
25	AP(5)	Area above areal profile level 5	Pixels	
26	AP(6)	Area above areal profile level 6	Pixels	
27	AP(7)	Area above areal profile level 7	Pixels	
28	AP(8)	Area above areal profile level 8	Pixels	
29	BLEND	Deblending flag		see text
30	QUALITY	Quality flag		see text
31	N(0,1)	Profile classification statistic	$\sigma \times 1000$	see Section 2.2.3
32	PRFMAG	Profile magnitude	Millimag	see Section 2.2.3

Table 1. The full 32-parameter Image Analysis Mode set for each detected image, along with units for internal storage as 4-byte integers.

and intensity-weighted parameters being calculated and recorded. The object catalogue produced for each plate consists of an unformatted binary file (the Image Analysis Mode, or IAM, file) of record length 128 bytes consisting of 32 4-byte parameters per object; depending on Galactic latitude and plate depth, this individual plate catalogue can have anything from 10^5 to 10^7 entries. Table 1 details the full 32 parameter set available for each image. Note that parameters 1,2,19,20,31 and 32 and some bits in parameter 30 are derived at a second stage of processing (known colloquially as ‘post processing’ – see Section 2.2) Most of the parameters in Table 1 are self-explanatory and are derived directly from first- and second-order moments as described in Stobie (1986). However, the following gives further details of some of the more esoteric parameters:

- COSMAG (parameter 9) is calculated from the sky-subtracted intensity values in the connected pixels comprising an image,

$$\text{COSMAG} = \{-2.5 \log_{10} \sum_{i=1}^n (I_i - I_{\text{SKY}})\} \times 10^3, \quad (4)$$

and is given in units of millimag. COSMAG is an isophotal magnitude.

- BLEND: each image is deblended by rethresholding at the levels defined by Equation 2, Beard et al. (1990); at each level, the connected pixels are examined for fragmentation

and pixels are assigned to fragments using the algorithm described therein. Images which have been deblended have this indicated in the deblending flag. A code of $-n$ means the image is the parent image of n components, while a code of $+n$ means that the image is the n^{th} deblended component (or child image) of a parent image. Both parents and children are retained in the IAM datasets of each plate in the SSS.

- QUALITY is an integer flag of 32 bits that are used to record situations encountered during the analysis of the pixels comprising an image. Bits are set in such a way that increasingly severe conditions are flagged by setting increasingly significant bits in the quality flag. Table 2 gives more information; other bits in the quality flag are either used only for image analysis software debugging or are totally unused.

2.2 Post-processing

The post-processing of each field consists of a number of separate tasks that either overwrite information into the individual plate catalogue files, or that write separate files of data or coefficients. Paper I describes the SSS database organisation and the system that is used to associate individual plate files into a seamless whole. Here, we describe the post-processing tasks that operate on each plate datafile to

Event	Bit set	Incr- ement	Severity	Comments
Orientation calculation failed	0	1	Information	Image perfectly round
Ellipticity calculation failed	1	2	Information	Image perfectly straight
Image too multiple for deblending	2	4	Warning	Image split into too many fragments
Bright image	4	16	Information	Image has pixels brighter than highest areal profile level (as defined by $n = 8$ in Equation 3)
Large image	6	64	Warning	Image has area greater than maximum specified for deblending
Possible bad image	7	128	Warning	Image is in region likely to be affected by step wedge or label (see Section 2.2.2)
Image near very bright star	10	1024	Warning	Image may be spurious due to bright star (see Section 2.2.2)
Image touches boundary	16	65536	Severe defect	Image may be partially missing

Table 2. IAM parameter 30 (quality flag) details.

produce astrometric, photometric and image quality/class information.

2.2.1 Astrometry: parameters 1,2 and 20

Paper III describes the derivation of global astrometric solutions for each plate. IAM parameters 11,12 and 18 (respectively x , y and ellipse-fit position angle with respect to the x axis) are transformed into celestial co-ordinates and a celestial position angle which are written to IAM parameters 1,2 and 20 respectively. Proper motion information is also derived between J/R plate pairs and held in separate files, as described in Paper III.

2.2.2 Additional quality information

Two additional bits in the quality flag that are unused by the image analysis software are derived at the post-processing stage. Firstly, bit 7 is used to flag images that are in parts of the plate that are likely to be affected by the presence of step-wedges and labels. Areas of the plate are flagged in this way based on the number and the telescope origin of the plate. For example, all UK Schmidt plates have a 7-step wedge in the west of their northern edge; in addition plate numbers 1 through to 5715 have a 7-step wedge on their eastern edge; plate numbers 5716 through to 6295 have a 16-step KPNO wedge in the same eastern position of the 7-step wedge while all plates numbered from 6296 have a 16-spot KPNO wedge in their south-eastern corner. The survey plate sets used have been examined for wedges and labels, and all images in the appropriate areas have bit 7 set to indicate possible spurious nature or probable poorly determined parameters in the case of real images. Because the modern survey field centres are spaced to provide $\sim 0.5^\circ$ overlap regions between adjacent plates, all parts of the sky affected by a wedge or label on one plate will be unaffected on one or other of the adjacent plates, so these flags are used when creating ‘seamless’ catalogues across plate overlap boundaries when making a decision as to which image to include out of a set of duplicates (see Paper I).

Secondly, possible problems with an image due to the proximity of a very bright star are indicated using bit 10. Tritton (1983) describes in some detail the origin and appearance of various image defects around bright stars on

sky-limited UK Schmidt plates. While the background following algorithm is tuned to minimise spurious image detections around bright stars, there are inevitably many false detections due to, for example, diffraction spikes. Within the SGC survey, 10 plates from each survey colour were examined by eye to measure an exclusion radius, as a function of magnitude, around bright stars. In Figure 1 we show these measurements and the log-linear fit as a function of magnitude that is used to flag images as potentially spurious. We have been conservative in this procedure in the sense that we have flagged all images that could *possibly* be spurious, including of course some real images. Hence, if a relatively uncontaminated (but incomplete) catalogue is required to be extracted from the survey data, this quality bit can be tested. The flagging procedure is completely automatic: given the fit as a function of magnitude and a brightness threshold above which to apply it, a list of bright stars is extracted from each IAM dataset and a record kept of the magnitude and radius for flagging. These lists are recorded for each field and can be used for estimating spatial sampling completeness when employing this flag.

2.2.3 Image classification

The SSS data are image classified using a two-stage classification scheme originally developed for APM data (e.g. Irwin & McMahon 1992). The first classification stage makes use of conventional techniques such as surface brightness and image shape (cf. Heydon-Dumbleton, Collins & MacGillivray 1989; MacGillivray & Stobie 1984). The second stage uses a series of image parameters to trace the stellar locus in a multidimensional parameter space and then quantify the similarity, or otherwise, of an individual image with respect to stellar objects of the same intensity. Advantages of this second stage include: the generation of a ‘linearised’ instrumental magnitude scale (see later); the ability to incorporate prior knowledge of the expected fraction of different classes of images; and a stellarness index in addition to the more usual discrete classification flag (stellar/non-stellar/noise). The stellarness index quantifies how well the parameters of a given image match the stellar template for that intensity. For ease of use, the index is given in terms of the equivalent normalised Gaussian distribution, of zero-mean and unit-variance – ie. an $N(0,1)$ statistic.

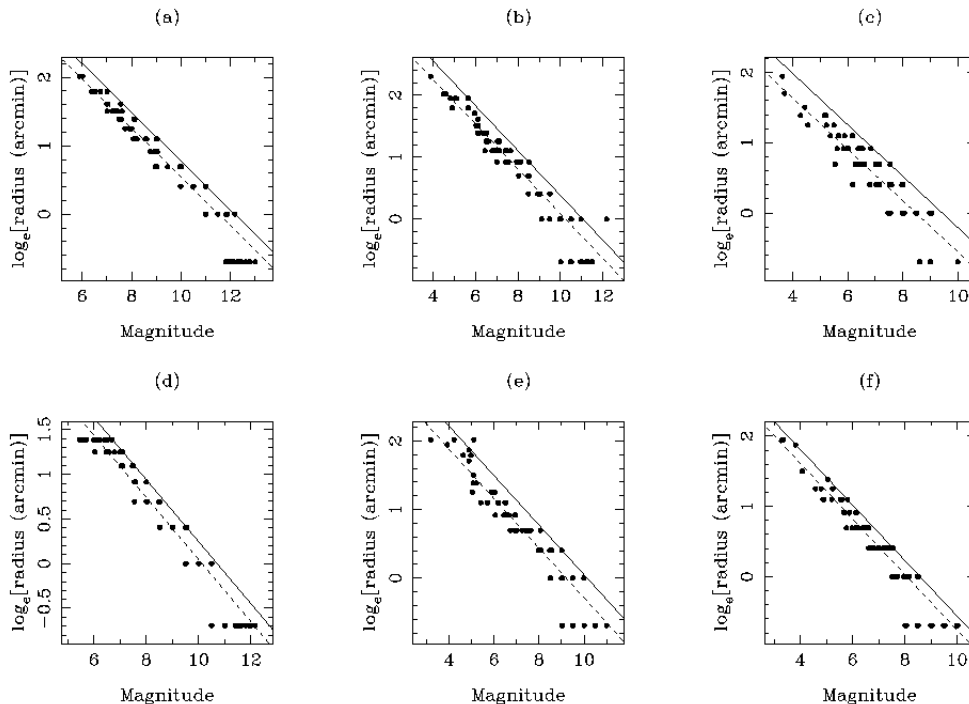


Figure 1. Exclusion radii as a function of magnitude for (a) SERC-J/EJ; (b) SERC-ER/AAO-R; (c) SERC-I; (d) AAO-R on 4415 film; (e) ESO-R and (f) POSS-I E surveys. The dashed lines are linear least-squares fits to the data while the solid lines are parallel to the fits but offset upwards to provide a conservative exclusion radius. Objects within the exclusion radius of a bright star have bit 10 set in their quality flag to indicate possible spurious nature.

The first stage of image classification consists of generating scatter plots using a combination of measures of the image magnitudes, surface brightness and peak brightness versus magnitude and automatically locating the stellar locus in each. The stellar loci are automatically found by converting each scatter plot into a 128×128 two-dimensional map, where each “pixel” represents the number of points lying in that bin. Obvious noise-like objects, for example with ellipticity >0.9 or with areal profile slopes incompatible with real images, are not included in the two-dimensional count (but are shown in the scatter plots). The location of the mode, and scatter about the modal value, are then determined, where possible, for each magnitude/peak slice and used to track the stellar locus and spread in stellar locus. For faint magnitudes where the stellar locus blends in with the remaining object loci, the centre-of-gravity of the generic distribution is used instead.

Figures 2(a) to (c) show typical examples of these scatter plots, where the solid lines mark the boundaries of the stellar/non-stellar locus – defined to be 2σ away from the mode, where the mode is well measured, or defined as the centre of gravity of the distribution for the faint end. The isophotal area versus magnitude diagram is additionally used to define a stellar/noise image boundary which is further used to flag images not to consider in the other two plots. After some experimentation, a combination of the three scatter plots shown in Figures 2 was found to give a reliable stage-1 classification over a wide range of magnitudes, Galactic location and plate/emulsion combinations.

The final stage 1 classification is based on a combination of the signed sigma-normalised distances from the stellar

loci from these three plots plus the image ellipticity information. As noted previously, at this stage the stellar/non-stellar boundary is set to conservatively class objects as stellar by defining a 2σ boundary from the median stellar locus. In a final step, obvious non-stellar objects in the stellar bin are rebadged by checking for consistency of other parameters such as ellipticity and areal profile slope.

At the completion of the first stage of image classification, each image has IAM parameter 19 overwritten by a classification code in the range 1 to 4 where 1=non-stellar, 2=stellar, 3=unclassifiable and 4=noise (i.e. images lying above the upper locus in Figure 2a.)

The provisional classification from stage 1 is then used as the primary input for the stage 2 classification scheme outlined earlier. This second phase builds upon the classification already developed by using it as the basis for deriving a more general descriptor of image shape. Providing the stage 1 stellar sample is a fair representation of the total stellar population, and only has modest contamination by non-stellar images, it is feasible to use it as a means to automatically track the stellar locus for any combination of the measured SuperCOSMOS image parameters.

Automatically deriving both the position and spread in the stellar locus as a function of magnitude, for any of the image shape parameters is straightforward, even with modest amounts of non-stellar object contamination, providing robust estimation techniques are used (e.g. Hoaglin, Mosteller & Tukey 1983). For any desired image shape descriptor, the location of the median of the population suffices to define the locus as a function of magnitude, while the median of the absolute deviation from the median (MAD)

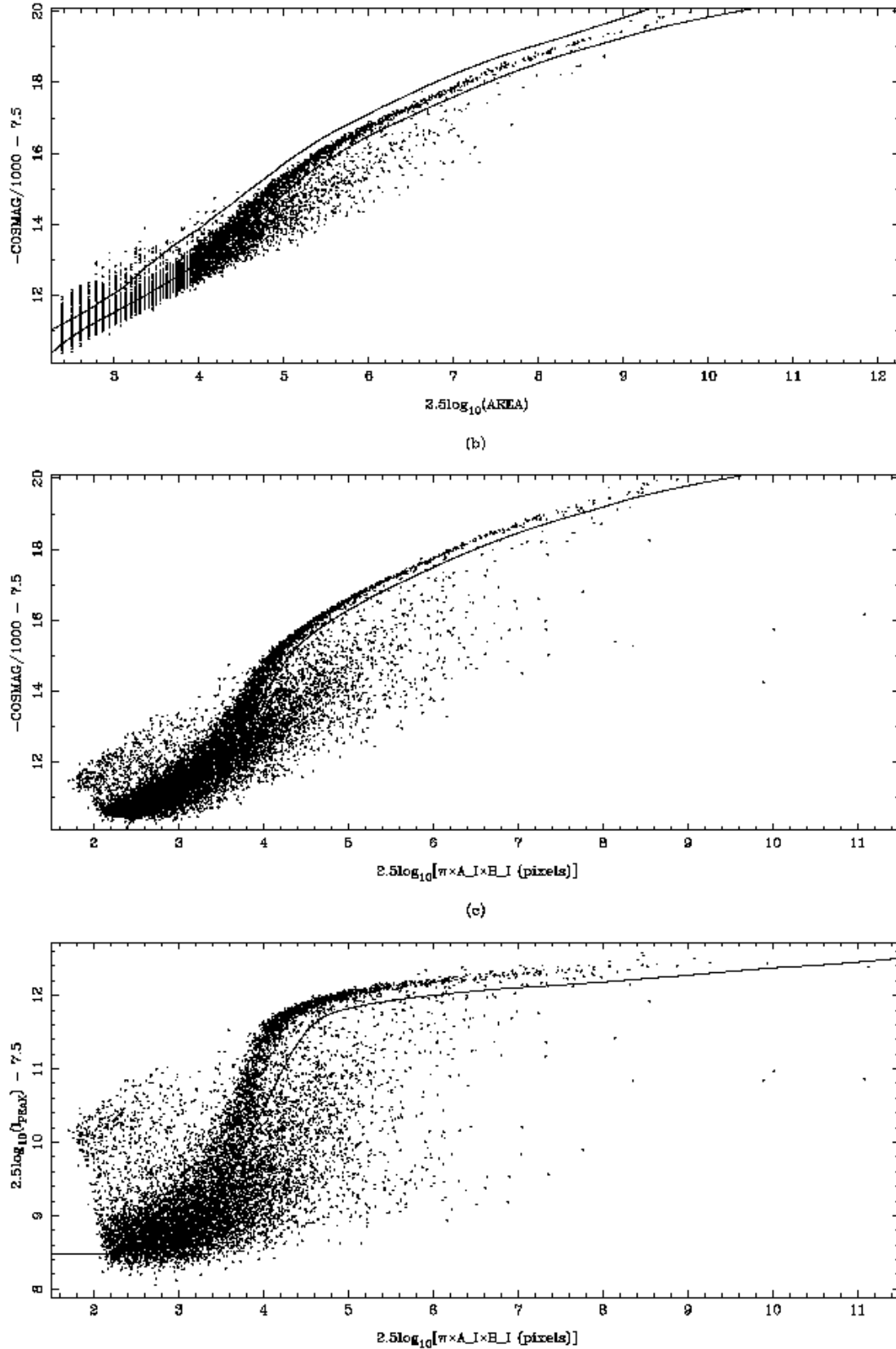


Figure 2. Scattergrams of image magnitude/peak brightness versus unweighted/weighted area used at the first stage of image classification.

provides a good measure of the scatter about this locus. The MAD estimate of scatter can then be converted to the equivalent Gaussian sigma by noting, as before, that $\sigma_{\text{Gauss}} = 1.48 \times \text{MAD}$. By this means each of the individual image shape descriptors can be renormalised to follow a zero-median, unit-variance Gaussian-like $N(0,1)$ distribution.

Another part of the second stage of image classification consists of an iterative determination of the stellar radial profile (ie. the stellar point spread function, PSF, for the plate) and the determination of a linear instrumental magnitude scale. This follows the procedure described by Bunclark & Irwin (1983) and makes use of the fact that, to a good approximation, all stellar images should have the same intrinsic profile shape whatever their magnitude. The areal profile measures (Equation 3) form the basis for this estimate, using the preset instrumental profile threshold levels as a first guess for the intensity scale. Figure 3 shows the results of a typical profile determination and linearised transfer function between isophotal and profile magnitude for a survey plate. The resulting stellar PSF can then also be used as part of the classification scheme.

In order to make an optimal judgement about the class of an object, a traditional Bayesian classification scheme uses knowledge of the conditional and prior probabilities on the right hand side of the following equation

$$p(s|d) = \frac{p(d|s)p(s)}{p(d|s)p(s) + p(d|g)p(g) + p(d|n)p(n)} \quad (5)$$

where the probability, or likelihood, of observing the image descriptors for stars, galaxies and noise are given by $p(d|s)$, $p(d|g)$ and $p(d|n)$ respectively; $p(s)$, $p(g)$ and $p(n)$ are the respective prior probabilities of finding a star, galaxy or noise image; and $p(s|d)$ is the posterior probability of the image being a star. In a similar way we can write equations for $p(g|d)$ and $p(n|d)$, the posterior probability of the image being a galaxy or noise object.

Unfortunately, the distribution of both galaxy and noise image parameters is in general unknown, implying that we cannot directly use a Bayesian estimator in this case. The problem is further compounded by the fact that the real likelihood function for stellar images is also non-trivial to estimate. This is caused by the underlying error distribution of the parameters being non-Gaussian in the real world and also because the image parameters are highly correlated, with the degree of correlation varying significantly as a function of magnitude.

However, deriving the stellar PSF as part of the internal intensity calibration helps to significantly reduce the number of free parameters required to accurately describe the shape of an object. Each image has (up to) 8 parameters measuring the areal profile which can be readily converted into the equivalent radial profile. Clearly, images with derived radial profiles significantly steeper than the stellar PSF are more likely to be noise images, while those with derived profiles much shallower than the stellar PSF are more likely to be galaxies. After some experimentation we found that the intensity-normalised slope of the sigma-weighted difference between an image radial profile and the stellar PSF provided a way of summarising the stellarness of an image using all the areal profile information. This measure preserves both the ‘sign’ of the deviation and quantifies the

difference. The normalised-slope measure is then combined additively with (the relatively) independent information derived from the intensity-weighted second moments and peak intensity to produce a single number measure. Finally, as a function of magnitude, all objects previously classified as stellar, are used to convert the stellarness index back to a zero-median unit-variance $N(0,1)$ score. This stellarness index is our pragmatic equivalent of the likelihood function of the data and summarises the probability that the observed data arose from a stellar object.

A typical example of the derived stellarness index for a survey plate is shown in Figure 4 with the primary stellar locus boundaries adopted ($+2\sigma$ for star/galaxy and -3σ star/noise). As a further refinement this average value of the stellarness index as a function of plate position is tabulated and used to remove small variations in the zero-point of the stellar locus caused by field effects.

Returning to the idealised Bayesian scheme outlined previously, for star/galaxy separation the main quantity of interest is

$$\frac{p(s|d)}{p(g|d)} = \frac{p(s)p(d|s)}{p(g)p(d|g)} \quad (6)$$

since when this ratio is greater than unity the object is classified as a star, and when less than unity as a galaxy. Although the underlying distribution, $p(d|g)$, is unknown, we do know that both galaxy and noise images have a much wider spread of image shape descriptors than stars, hence to a reasonable approximation $p(d|g) = U(a, b)$ and $p(d|n) = U(c, d)$; where U denotes uniform distribution and the arguments the range over which it applies – which in general are a function of magnitude. In the absence of prior information the ratio of $p(s|d)/p(g|d)$, if $p(g|d) = U(a, b)$ and one end of the range (a, b) lies within the normal stellar distribution, is exactly equivalent to specifying a one-sided k-sigma boundary separating stars from galaxies.

The prior information only enters via the ratio of the expected numbers of star:to:galaxies at a particular magnitude. For most survey fields (i.e. not the Galactic Plane) the total number of stellar images and the total number of galaxy images visible on a survey plate are roughly equal. As a function of magnitude, however, the stellar population varies roughly as $n(m) \propto 10^{0.25m}$ while the number of galaxy images varies as $n(m) \propto 10^{0.45m}$. Using the equality of total numbers of star and galaxies near the plate limit to define the relative normalising constant, automatically specifies the ratio $p(s)/p(g) = \text{constant} \times 10^{-0.2m} = 10^{-0.2(m-m_{\text{ref}})}$ for all magnitudes. This prior information ratio can then readily be incorporated into the previous boundary definition by defining a new k'-sigma boundary using the assumed $N(0,1)$ distribution of the likelihood function to convert ratios to sigmas.

Although inevitably somewhat adhoc, this scheme does allow us to fold in additional information within the framework of a Bayesian approach (e.g. prior knowledge of star:to:galaxy ratios and the knowledge that galaxies and noise images have a wide range of image shapes). The advantages of decision making directly in k-sigma space are that it is straightforward to place realistic constraints on the influence of the prior knowledge, i.e. by limiting how much the boundary can shift, and it also mitigates against

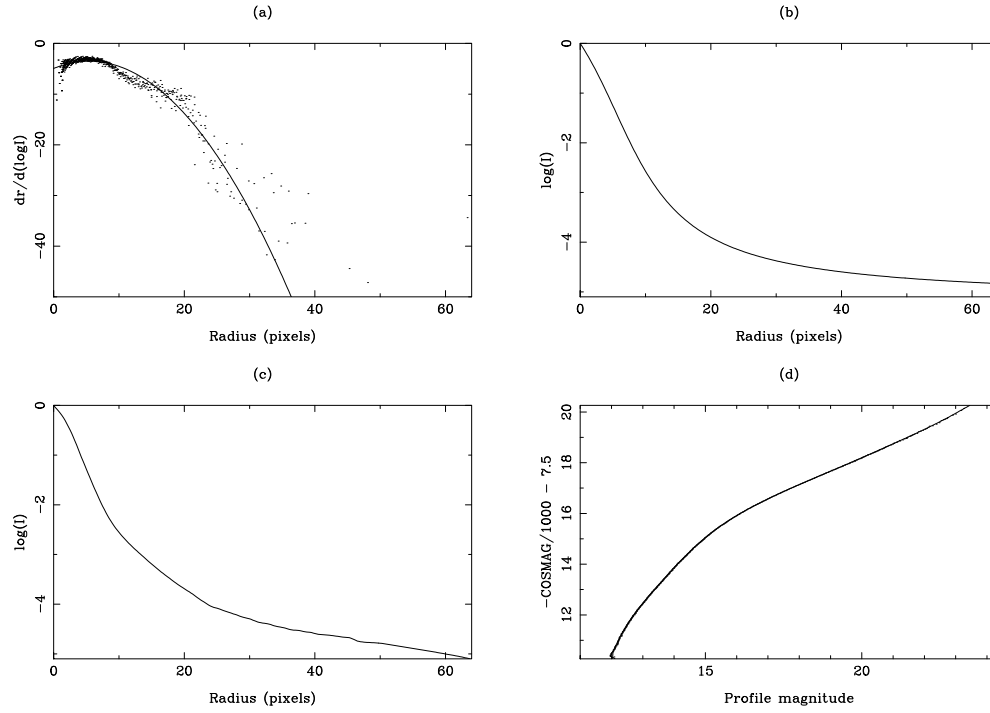


Figure 3. Results of the iterative determination of the stellar profile for a typical plate: (a) differential profile estimate; (b) initial profile; (c) iterated profile; (d) transfer function of isophotal to profile magnitude (see Bunclark & Irwin 1983).

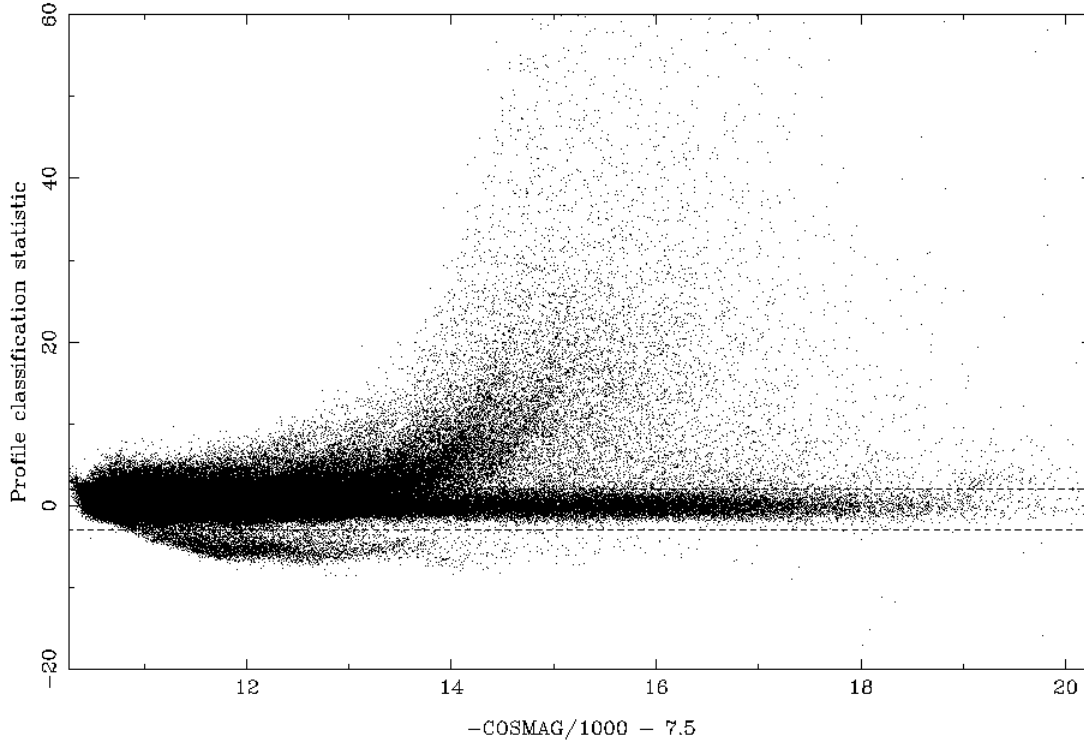


Figure 4. Scatter plot of the profile classification statistic for a typical survey plate. This indicates the residuals (in terms of a zero mean and unit standard error quantity) of each image's areal profile set when compared with an average stellar template. The boundaries indicate the position of all objects finally classed as stellar. Broadly speaking, objects with steep radial profiles (hard, noisy images) have low values, while objects with shallow radial profiles ('fuzzy' images, more often than not galaxies) have high values. An object matching the stellar template perfectly has a value of zero.

Survey	No. of fields	Gradient of profile scale		
		min	max	mean $\pm\sigma$
SERC-J/EJ	25	1.133	1.456	1.281 ± 0.080
AAO-R/SERC-ER	19	1.118	1.239	1.178 ± 0.028
SERC-I	6	0.947	1.156	1.086 ± 0.074
ESO-R	14	1.038	1.179	1.107 ± 0.044
POSS-I E	11	0.956	1.212	1.070 ± 0.081
AAO-R on 4415 film	4	1.182	1.297	1.243 ± 0.044

Table 3. Gradients of the profile magnitude scale for the various types of survey plate comprising the SGC dataset.

the effect of non-Gaussian errors by automatically scaling the boundary using a robust sigma estimator.

2.3 Photometric calibration

The isophotal instrumental magnitude scale for IAM data is non-linear with respect to external apparent magnitude. Non-linearities are introduced by, for example, thresholding and the limited dynamic range of the measuring machine in addition to any non-linearities inherent in the photographic characteristic curve with respect to the linear $D - \log I$ scale assumed. Additionally, the magnitude scale for galaxies will be, in general, different to that of stars. The reason for this is that galaxies are generally more extended and of lower surface brightness than stars, and as such have integrated magnitudes that are less susceptible to any dynamic range limit during measurement. Moreover, the linearised profile magnitude for stars is easier to calibrate than the isophotal scale when external calibration data are limited since it is better behaved. Note that the profile magnitude for a non-stellar object is not useful since such objects have, of course, non-stellar profiles. For these reasons, the stellar/non-stellar magnitude calibrations for the survey data are treated separately. The calibration procedure adopted was as follows:

2.3.1 Gradient of the instrumental stellar profile magnitude scale

For each of the survey colours (e.g. SERC-J, ESO-R) the gradient of the faintest 7 mag of the profile magnitude scale was measured against CCD data from Boyle, Shanks & Croom (1995) and Croom et al. (1999). Throughout this paper, where any comparisons have been done between photographic and photoelectric photometry, colour equations from Blair & Gilmore (1982), Bessell (1986) and Evans (1989) have been used to naturalise the magnitudes to the photographic $B_J/R_{63F}/R_{59F}/E_{2224}/I_{IVN}$ systems. The results of the measurements are shown in Table 3, where the number of plate gradients and a standard error estimate are also given. We found that the RMS residuals of the linear fits between the profile and standard magnitudes were in the range 0.1^m to 0.2^m , in line with expectations for photographic photometry of fainter stars and also demonstrating that the profile magnitude scale has no increased scatter over that present in the raw isophotal scale (e.g. Bunclark & Irwin 1983). The mean gradients in Table 3 are reasonably close to unity with small standard errors. This implies that

the assumed calibration used for transmission to intensity was a reasonably good one. Furthermore, the small scatter in the gradients means that rough calibration to the plate limit is possible on a field-by-field basis using a small number of relatively bright standards in each field to define a bright stellar calibration curve that can be extrapolated to the plate limits. Figure 5 shows a typical example of a deep photometric sequence plotted against the linearised profile magnitude scale, demonstrating how closely linear the profile scale is over many magnitudes above the plate limit. Contrast this with the same plotted for the isophotal scale, which is non-linear at the 0.5 mag level.

2.3.2 Rough profile magnitude calibration for stars

In order to roughly calibrate the stellar profile magnitude scale of each field with respect to external standards, a compilation of BV photometry over the whole sky was made by combining the Tycho Catalogue (ESA 1997) and the Guide Star Photometric Catalogue I (Lasker et al. 1988). This provided two colour photometry down to $V \sim 15$ in every survey field. Standard magnitudes in the RI bands have been estimated from relationships between (B-V) versus (V-R) and (V-I) derived from the multicolour standard star data of Landolt (1992). For each field, a calibration curve of the profile instrumental magnitude versus naturalised standard magnitude was derived. Figure 6 shows a typical example for the survey data. The solid lines are least-squares fits to the data, with the added linear constraints that at a fixed point 3 mag fainter than the faintest calibrating standard, the gradient is set at the appropriate mean value given in Table 3 while the second derivative of the fitting function is set to zero. In this way, the calibrating function can be linearly extrapolated from this point to the plate limit, and the calibrating function has no discontinuities in itself or its first derivative. This somewhat complicated procedure is an attempt to realistically model the shape of the ‘linearised’ stellar profile magnitude scale, which is indeed linear over its faintest 7 mag range (e.g. Figure 5), but which departs from linearity brighter than this due to the fundamental dynamic range limits of the machine as dictated by diffraction-limited performance in the imaging optics and the transmission digitisation range, along with the dynamic range limit of the photographs themselves.

The fact that the calibrations are extrapolated for the fainter magnitude range coupled with the paucity of external calibrating stars on the linear part of the profile scale results in small (10% to 20%) errors in the zeropoint of the faint magnitude calibration of each field. This problem is dealt with in the next Section.

2.3.3 Global zeropoint definition

All the Schmidt surveys have varying degrees of overlap between adjacent fields. For the POSS-I E and ESO-R surveys, this overlap can be very small (or non-existent in the case of a few adjacent ESO-R fields), but for the UK Schmidt surveys the field centres were chosen to give $\sim 0.5^\circ$ overlap strips for all fields (this system of field centres, reflected into the northern hemisphere, has been adopted for the POSS-II survey). These overlap regions can

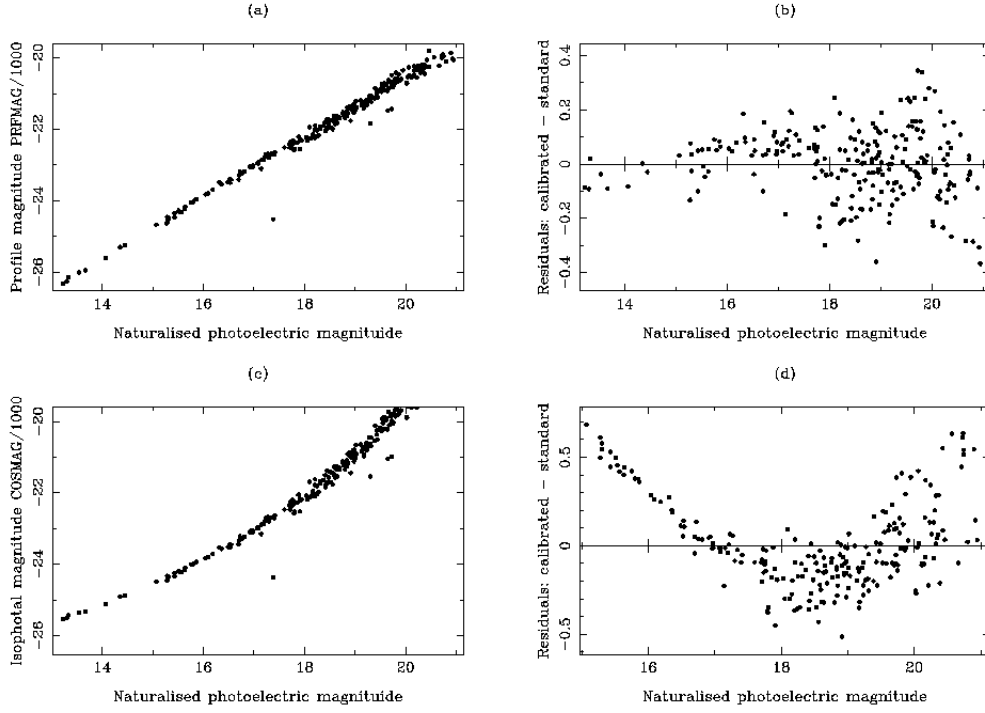


Figure 5. Plots of naturalised photoelectric magnitudes versus (a) profile magnitude and (c) isophotal magnitude for R band data in survey field 413. Panels (b) and (d) show the non-linear components after linear least-squares regression fits. The profile scale is closely linear over ~ 8 mags. The isophotal scale is non-linear at the level of > 0.5 mag; furthermore, such non-linearities are not repeatable from field to field.

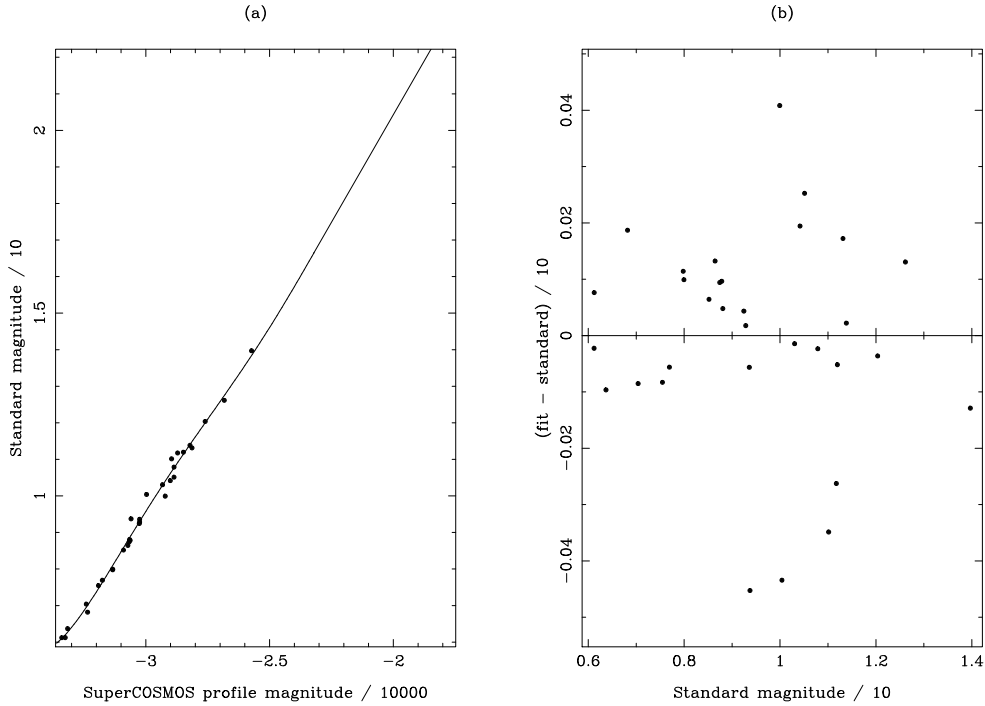


Figure 6. Calibration curve of the linearised stellar profile magnitude scale versus external photoelectric photometry naturalised to the photographic system. The solid line in (a) is a least-squares polynomial fit constrained to have the required gradient at the faint end. In (b) we show the residuals of the data about the fit.

be used to define a set of individual field photometric zero-points such that the mean difference over all stars between the stellar magnitudes from the two measurements available per star in any given overlap region is zero. Consider any two adjacent fields m and n . The mean (systematic) difference between the stellar magnitudes in the overlap region is $\Delta_{nm} = z_n - z_m$ where z_n and z_m are the unknown zero-points. A mosaic of many fields gives a (singular) set of equations in the Δ and z values. Such a set may be solved by singular value decomposition to yield minimal zero-points that solve the set. However, we have used faint CCD photometry to externally fix as many zero-points as possible over the survey region. This makes the equation set non-singular and yields a unique vector of zero-points that are tied to an external system. This procedure is similar to that adopted by Maddox, Efstathiou & Sutherland (1990) for the APM Galaxy Survey except that we have *not* solved for the field-to-field differences in the gradients of the photometric scales. Also, our sources of external CCD photometry included data from the Guide Star Photometric Catalogue II (Postman et al. 1997), Boyle et al. (1995), Croom et al. (1999), Cunow et al. (1997) and references therein, unpublished data used in the calibration of the Edinburgh-Durham Southern Galaxy Catalogue (e.g. Nichol 1993 and references therein) and Stobie, Sagar & Gilmore (1985) in addition to that published in Maddox et al. (1990). At the time of writing, approximately 50% of all southern hemisphere fields have external CCD data defining their photometric zero-point.

2.3.4 Correction of systematic errors in stellar colours as a function of magnitude and plate position

The photometric calibration of photographic plates based on calibrating stars necessarily assumes that there exists a unique calibration curve that is applicable over the entire plate. In general, this is *not* the case. For example, graphs of external photoelectric magnitude versus internal linearised profile magnitude, as a function of plate position, show significant changes in gradient. One possible cause of this is that the response of the photographic emulsion is not uniform over the plate – i.e. the characteristic curve of the emulsion is not constant. Whatever the cause, the results are the same: systematic errors in photometry as a function of magnitude and position occur, and those errors manifest themselves most visibly when magnitudes are combined to generate colour indices. Moreover, we have assumed a constant value of the gradient of the profile magnitude scale in any given passband, and as Table 3 shows there is a significant dispersion about the mean values adopted which adds to any systematic effects within a given plate. For example, Figure 7 shows an I versus (R–I) colour–magnitude diagram for survey field 758. There is apparently a trend for brighter stars to get become bluer in this diagram, along with a significant increase in scatter about the modal colour for brighter magnitude ranges. These effects are both due to systematic errors in photometry as a function of magnitude and position. Furthermore, Figure 8 shows a stellar (J–R) versus (R–I) two-colour diagram for a mosaic of 9 fields at the South Galactic Pole for the magnitude range $17 < B_J < 18$. While the general trend of red objects being red in both colours is apparent, it is also true that stars having interme-

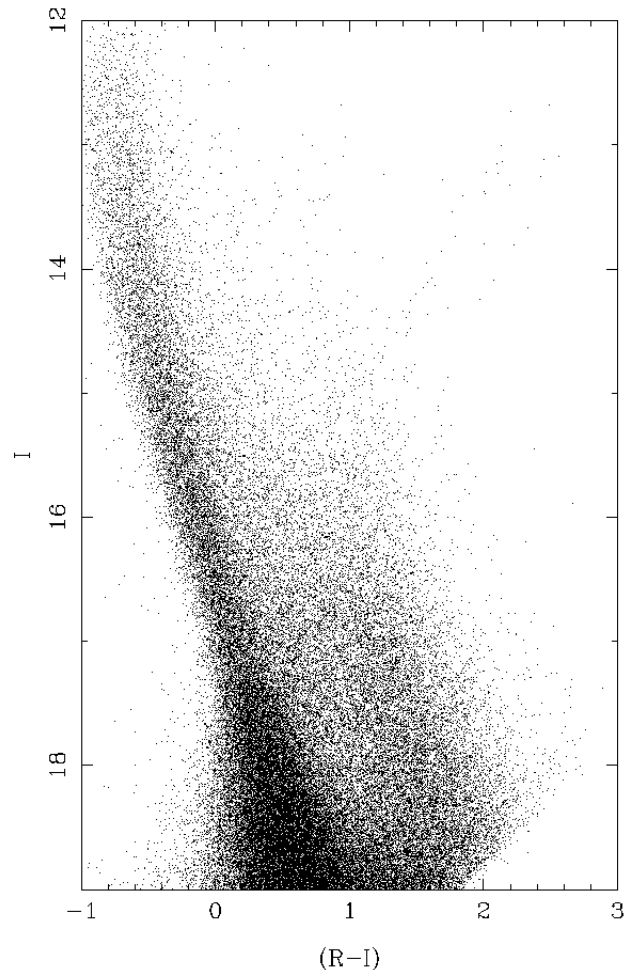


Figure 7. Stellar colour–magnitude diagram (I versus R–I) for survey field 758 *before* correction of systematic colour errors as a function of magnitude and position. There is no strong reddening in this high latitude field, so the large colour change with magnitude has to be due to systematic calibration errors.

diated colours do not show a good correlation between (J–R) and (R–I). The scatter in Figure 8 is rather large, and masks astrophysically useful information.

These problems have been documented in the past (e.g. Hambly et al. 1995; Goldschmidt & Miller 1998 and references therein). In the absence of large-scale external calibration sequences, there is no option other than to use the stellar distributions themselves (in colour, as a function of magnitude and position) to measure the size of these effects and to calibrate them out. Such corrections require that one passband is chosen as the standard with respect to which all other passbands are corrected. Here, we have chosen the J plates for this purpose because the most widely available external photometry is in the B band and we expect that the rough calibrations (Section 2.3.2) will be the most accurate in this passband. The correction procedure is straightforward, and is applied to each set of R and I field data individually. First, shifts in colour as a function of position are measured by cross-correlating smoothed histograms of number–colour counts as a function of magnitude and

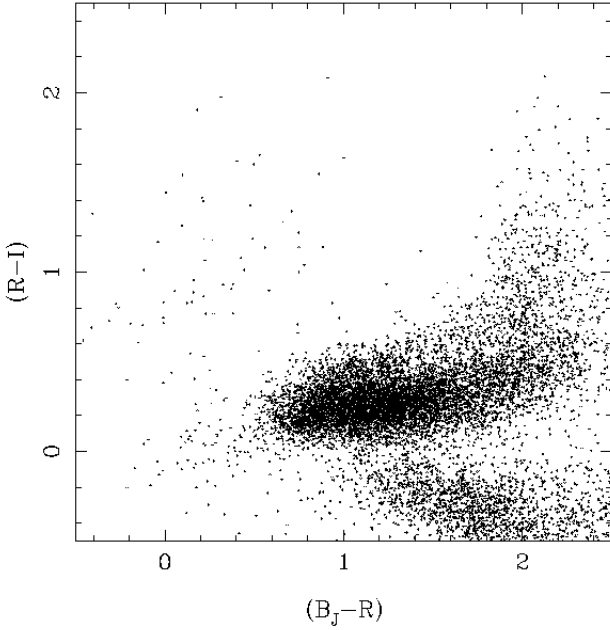


Figure 8. Stellar two-colour diagram (B_J-R versus $R-I$ in the magnitude range $17 < B_J < 18$) for 9 contiguous survey fields around the South Galactic Pole *before* correction of systematic colour errors as a function of magnitude and position.

Survey	Colour	Position of blue edge
AAO-R/SERC-ER	(B_J-R)	0.789
SERC-I	(B_J-I)	1.204
ESO-R	(B_J-R)	0.774

Table 4. Values of the 10th-percentile blue ‘edge’ used in fixing the survey colours (see text).

plate position in coarse bins of 1 mag and 2 cm respectively. The resulting data cubes of shifts are then padded, resampled onto a $3\times$ finer grid and linearly filtered and smoothed to yield final shift values to be applied to the data. The final stage of the correction procedure consists of forming number-magnitude histograms as a function of magnitude only, in 0.1 mag bins, and finding the 10th percentile blue ‘edge’ of the distributions. Hence, a shift of this value with respect to a global value (measured as the median 10th percentile blue edge of faint stars over all the fields in the survey) is measured and can be applied to the data to shift and straighten the blue edge to an internally consistent position. Table 4 shows the values measured over the whole survey for anchoring the colours in this way. Figures 9 and 10 show the results of this procedure for direct comparison with Figures 7 and 8. There is a significant improvement in the morphology and reduction in scatter in these diagrams after correction.

Of course, it should be noted that this procedure can potentially remove real astronomical features from colour-magnitude and two-colour diagrams. For example, differential reddening across a field would tend to be calibrated out by the above procedure. For this reason, the database access software (Paper I) allows the user the option of turning off

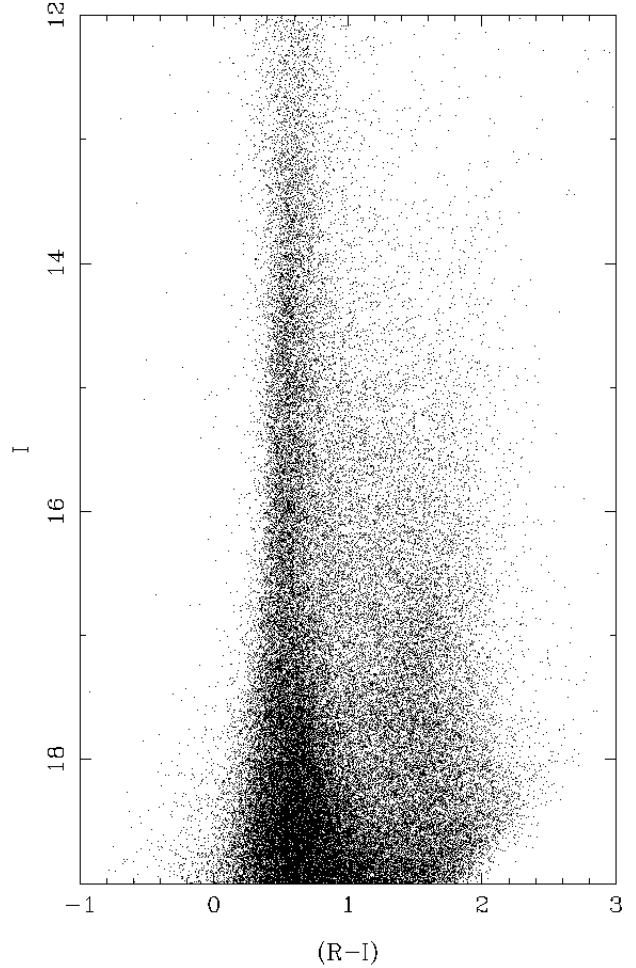


Figure 9. Stellar colour-magnitude diagram (I versus $R-I$) for survey field 758 *after* correction of systematic colour errors as a function of magnitude and position.

these corrections at access time so that uncorrected colours are available if required.

2.3.5 Galaxy (isophotal) magnitude calibration

As mentioned previously, the galaxy magnitude calibration must be treated separately to that of stellar objects. The isophotal magnitude scale is tied to that of stellar objects using the faintest 2.5^m range of objects where the isophotal scale for stars and galaxies is the same since at these magnitudes, the majority of galaxies are unresolved on the plates and have the same profile shapes. In order to apply a simple linear fit between isophotal and profile magnitudes, however, the isophotal scale must first be corrected for thresholding non-linearity (the profile scale is, of course, linear over much more than the faintest 2.5^m range).

The thresholding correction to the isophotal scale was modelled assuming a Gaussian profile,

$$I(r) = I_{\text{PEAK}} \exp(-r^2/2\sigma^2), \quad (7)$$

from which integration yields $I_{\text{TOT}} = 2\pi\sigma^2 I_{\text{PEAK}}$ where $\sigma = \text{FWHM}$ of the profile. If thresholding truncates the in-

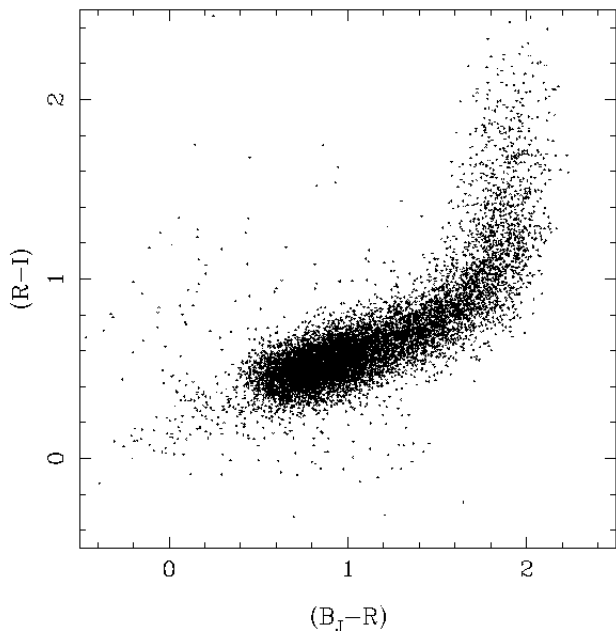


Figure 10. Stellar two-colour diagram (B_J-R versus $R-I$ in the magnitude range $17 < B_J < 18$) for 9 contiguous survey fields around the South Galactic Pole *after* correction of systematic colour errors as a function of magnitude and position.

egrated brightness at a radius r_t , then it is easy to show that

$$r_t^2 = 2\sigma^2 \log_e \left\{ \frac{100I_{\text{PEAK}}}{I_{\text{SKY}} \times \text{PCUT}} \right\}, \quad (8)$$

where I_{SKY} and PCUT are defined by Equation 2 in Section 2.1.4. We also have that the difference between the total and isophotal integrated intensities of an object is given by

$$\begin{aligned} I_{\text{TOT}} - I_{\text{ISOPHOTAL}} &= 2\pi I_{\text{PEAK}} \int_{r_t}^{\infty} \exp(-r^2/2\sigma^2) r dr \\ &= \frac{2\pi\sigma^2 I_{\text{SKY}} \times \text{PCUT}}{100} \end{aligned} \quad (9)$$

and defining an isophotal correction ϵ such that

$$m_{\text{CORR}} = m_{\text{ISOPHOTAL}} - 2.5 \log_{10}(1 + \epsilon), \quad (10)$$

it is straightforward to show that

$$\epsilon = \left\{ 1 - \frac{I_{\text{SKY}} \times \text{PCUT}}{100I_{\text{PEAK}}} \right\}^{-1} - 1. \quad (11)$$

Hence, a calibration of m_{CORR} versus the calibrated profile magnitude for the same image is possible, and is furthermore applicable to the full threshold corrected isophotal scale. Note that ϵ is not a correction to ‘total’ galaxy magnitudes (e.g. Young et al. 1998 and references therein) since such a correction is dependent on galaxy profile shape. Note also that we calibrate $m_{\text{CORR}} + 2.5 \log_{10} I_{\text{SKY}}$ to provide a first-order correction for vignetting and differential desensitisation as a function of plate position (e.g. Maddox et al. 1990). An example calibration of m_{CORR} versus calibrated profile magnitude is shown in Figure 11. In this way a calibration for non-stellar objects is defined in every field, this calibration being tied to the same external zeropoints as the stellar magnitude scale.

It is worth emphasising that the calibrations set up for

the survey photometry take the form of coefficients values that are applied to raw measurements as and when the data are accessed (see Paper I). This allows recalibration at any point in the future when better methods and/or better external calibration data become available. The raw, uncalibrated and uncorrected isophotal and profile instrumental magnitudes are also available, along with all morphological information produced during pixel analysis. This will allow, for example, investigation and implementation of more sophisticated galaxy calibration techniques in the future (e.g. Young et al. 1998 and references therein).

3 RESULTS AND DISCUSSION

When assessing the accuracy of the measurement, classification and calibration schemes detailed in the previous Section, it is important to distinguish between the various types of error that it is possible to measure and quote. This is particularly important when comparing the SSS characteristics against those of other survey programmes (e.g. Paper I). Here, we have assessed the internal consistency of the survey data by comparison between data for the same objects from overlap regions (i.e. where two independent measurements of the same quantity are available). Under the assumption that the two overlapping plates have the same characteristics of image quality and signal-to-noise ratio, this also provides estimates of the random errors (dividing by $\sqrt{2}$, where appropriate, for a single measurement). Note that similar comparisons in overlap regions other than those specifically used here yield similar results provided they have Galactic latitudes $|b| \geq 30^\circ$. As it will be shown in the next Sections, the random errors in single colour photometry are dominated by position and magnitude dependent systematic errors for brighter magnitude ranges, and it is therefore useful to quote an apparent ‘standard’ error in the presence of such effects, and also a relative error when comparing photometry within restricted magnitude and position ranges. The latter thus reflects the true, underlying random errors in the measurement process and is useful when the data are being used in isolation (for example, inter-comparison of object magnitudes) while the former is more appropriate when measurements are taken at face-value and compared with external data. Note however that the calibration procedure removes systematic errors in colour as a function of magnitude and position *and* across the survey as a whole (Section 2.3.4) so that the SSS object colours (e.g. B_J-R , $R-I$) are much more accurate than the external errors on individual passband magnitudes. This is illustrated later.

Of course, systematic errors can only be truly assessed with respect to external data that can be regarded as ‘gold’ standard, i.e. free from systematic error and having negligible random error, and we also describe comparisons against external CCD data that are of sufficient angular resolution and signal-to-noise that they can be regarded as error-free for these purposes.

3.1 Internal consistency and relative accuracy

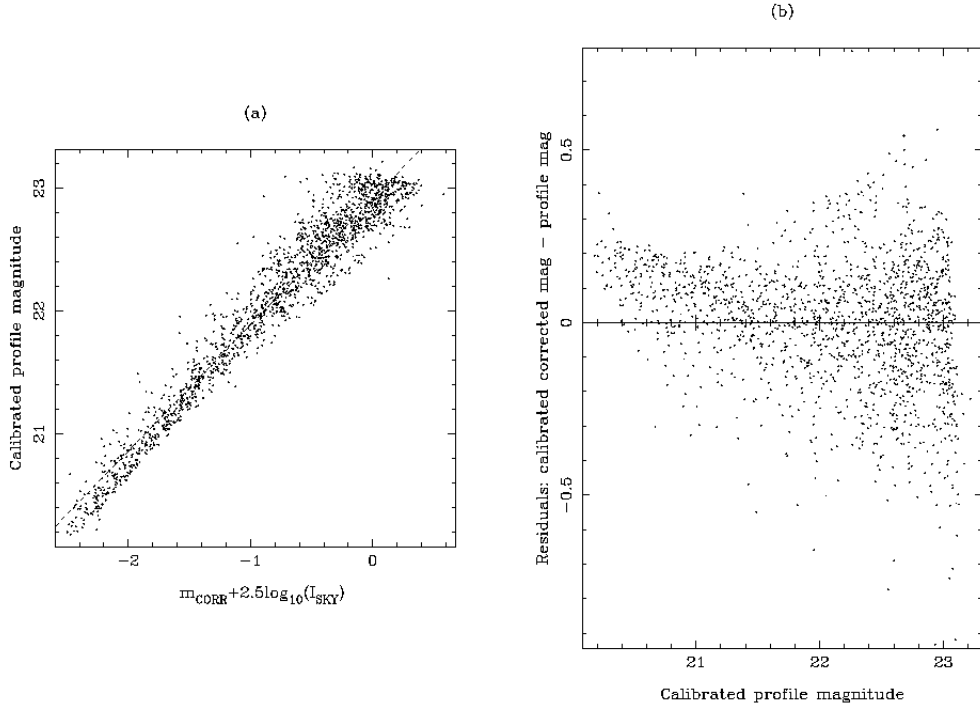


Figure 11. Calibration curve of the m_{CORR} (see text) for non-stellar objects versus calibrated profile magnitude for faint, unresolved images.

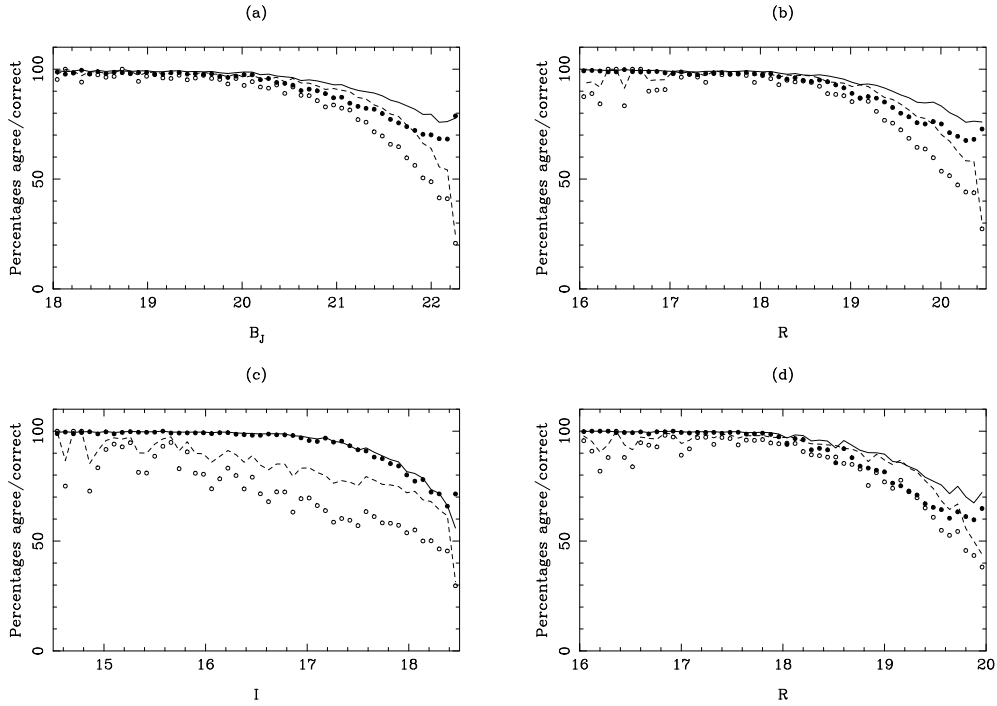


Figure 12. Classification scores when comparing data from two overlapping plates for (a) SERC–J/EJ, (b) AAO–R/SERC–R, (c) SERC–I and (d) ESO–R surveys. Solid circles are for stars while open circles are for galaxies; solid and dashed lines indicate the percentage accuracy of a single classification for stars and galaxies respectively (see text).

3.1.1 Image classification

In order to assess the consistency of the image classification, we compared data from each of the four survey types J,R,I and ESO-R in the large ($\sim 4^\circ$) overlap region between field numbers 292 and 241. In Figure 12(a) to (d) we show plots of the percentage agreement between the two independent classifications, as a function of magnitude, for stars (solid circles) and galaxies (open circles). These were analysed for the *underlying* correct classification for a single measurement using the following argument. Assume that there are just the two image classes, stellar and galaxian (the fraction of noise and unclassifiable images on any plate is always $\ll 1\%$). If we denote the probability that a real star is classified as such in any given magnitude range by $p_1(s|s)$ and the probability that a real galaxy is classed as such by $p_1(g|g)$ along with probabilities for incorrect classification by $p_1(s|g)$ and $p_1(g|s)$ (where the subscript refers to plate 1 and similar definitions are made for the overlapping plate 2), we have that for plate 1 for example

$$p_1(s|s) + p_1(g|s) = 1 \quad (12)$$

$$p_1(g|g) + p_1(s|g) = 1 \quad (13)$$

and similarly for plate 2. Between the two independent measurements, the probability of agreement for stellar class (for example) is equal to the sum of the probability that both measurements class a real star as such and the probability that both measurements misclassify a galaxy as a star:

$$p(\text{agree } s) = p_1(s|s)p_2(s|s) + p_1(s|g)p_2(s|g); \quad (14)$$

likewise for agreement on galaxian classification:

$$p(\text{agree } g) = p_1(g|g)p_2(g|g) + p_1(g|s)p_2(g|s). \quad (15)$$

Assume now that the noise parameters and general image quality of the plates are the same, i.e. write $p(s|s) = p_1(s|s) = p_2(s|s)$ etc. and since we are not interested in the cross terms in Equations 14 and 15 they can be eliminated using Equations 12 and 13 to yield

$$p(\text{agree } s) = p(s|s)^2 + \{1 - p(g|g)\}^2, \quad (16)$$

$$p(\text{agree } g) = p(g|g)^2 + \{1 - p(s|s)\}^2, \quad (17)$$

which is a set of two non-linear equations in the two unknowns $p(s|s)$ and $p(g|g)$. These are soluble using a simple iterative scheme, and in Figure 12(a) to (d) we plot the derived functions $p(s|s)$ (solid lines) and $p(g|g)$ (dashed lines).

From Figure 12, the image classification scheme is clearly working well, with stellar classification being *internally* repeatable/reliable at the $> 95\%$ level for magnitudes $B_J < 21$, $R < 19$ (or $R < 18.5$ for ESO-R) and $I < 17.5$. For galaxies, classification is reliable at the $> 90\%$ level in the ranges $17.5 < B_J < 21.5$, $15 < R < 19$ but is clearly not so good for the I plates. This is possibly due to the generally poorer signal-to-noise of I band Schmidt plates. Note that reliable image classification for all I images is of course available from the B_J data unless an object is severely reddened or intrinsically very red. It is important to emphasise that the only true test of the image classification reliability is against external data. This is because the above analysis cannot take into account any systematic effects (for example, classification of large numbers of faint, unresolved galaxies as stellar objects). Such a rigorous test is detailed

in Section 3.2.1. On the other hand, this internal test illustrates that the classification scheme is not severely limited by random errors at magnitudes as faint as $\sim 1.5^m$ above the respective plate limits.

3.1.2 Photometry (single passband)

Using the same overlap region as in the previous Section, we have compared the photometry to assess the internal accuracy of the photometric measurements and calibrations. Tables 5 to 8 give detailed accuracy figures as a function of magnitude for the J,R,I and ESO-R surveys respectively. In each Table, the figures for stars and galaxies are given separately since galaxy photometry will be less accurate at a given magnitude (e.g. Irwin 1985). The columns in each Table for each image type are the number of objects used in obtaining the measurements; the raw RMS (including any systematic effects); the median global zeropoint error; the RMS when this global zeropoint is removed; and finally the RMS when a position-dependent zeropoint is removed. Zeropoints as a function of position were determined from the data by taking median values over a scale size of ~ 2 cm (~ 20 arcmin) on the plates.

The following points should be noted from Tables 5 to 8:

- There are no systematic zeropoints at the faint end – this is of course a result of the plate matching procedure detailed in Section 2.3.3.
- There are increasingly large systematic errors for increasingly bright stellar magnitude ranges.
- Galaxy magnitudes are less susceptible to systematic effects than are stellar magnitudes.
- The *relative* precision of stellar magnitudes (i.e. within restricted position and magnitude ranges) is 5% or better when 3 mag or more above the respective plate limits.
- Relative galaxy magnitudes are, in general, worse than those of stars in a given magnitude range, as expected.

The systematic errors for bright stellar images are partly due to positional effects and partly due to the assumption of a mean gradient for the linear part of the profile magnitude scale. Since the gradient of the isophotal scale is also tied to this mean gradient, then systematic effects are also increasingly apparent in increasingly bright galaxian magnitude ranges due to the linear extrapolation from the faint levels at which the zeropoint is fixed. Section 3.2.2 shows some of these effects when comparing SGC photometry against an independent, external dataset.

Figure 13(a) to (j) illustrates some of these effects graphically, where we have plotted stellar J survey data in five magnitude ranges of 2 mag size in the range $13 < J < 23$. The left-hand panels show histograms of raw magnitude differences, while the right-hand panels show the underlying distributions of random errors left over after positionally-dependent systematic errors have been removed. Once again, the increase in random error, and decrease in systematic error, with decreasing brightness are apparent.

3.1.3 Photometry (colours)

Figure 14 shows the consistency of our survey colours J-R (with R from both UK and ESO Schmidts) and R-I in

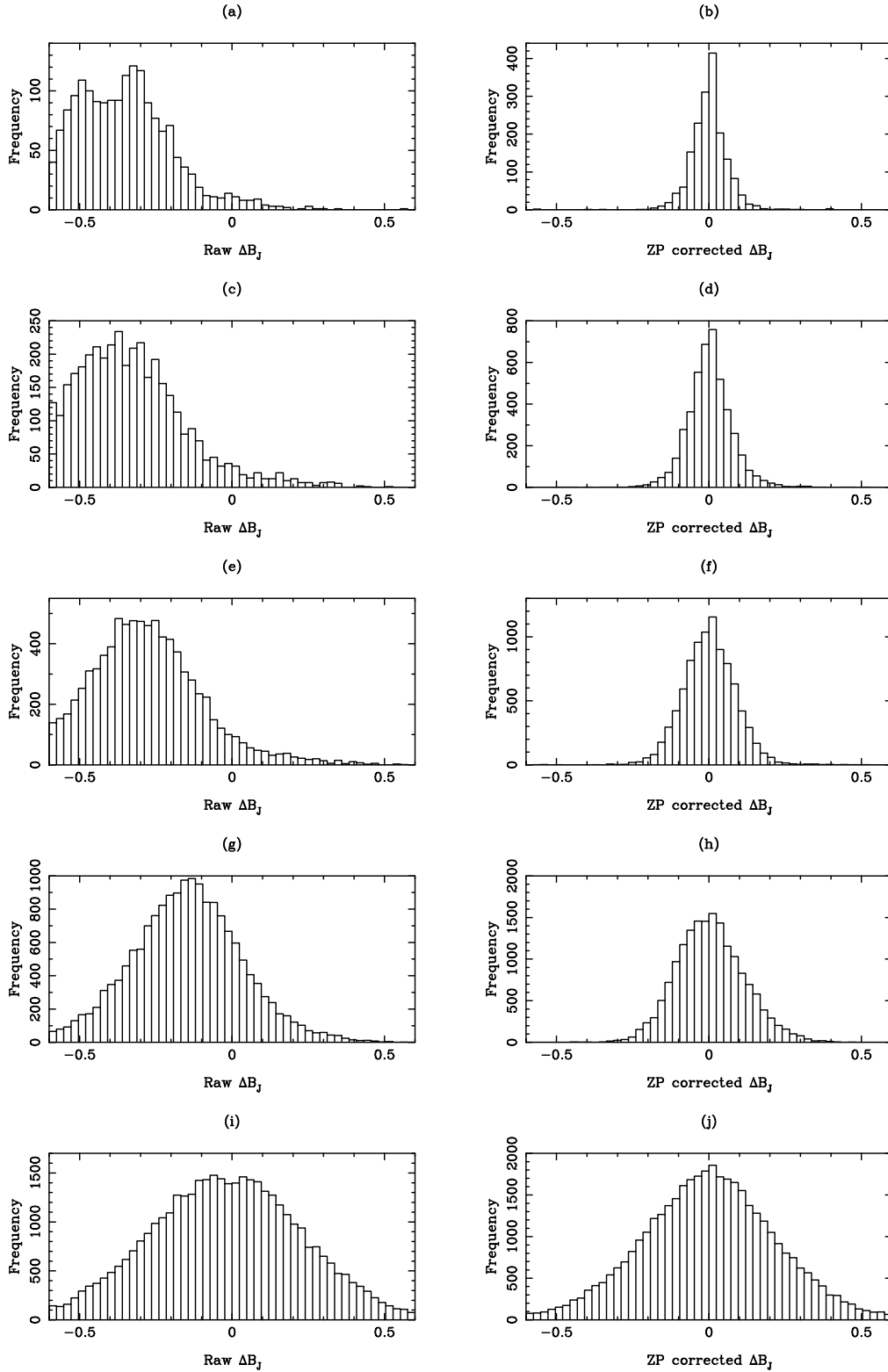


Figure 13. Histograms of differences between J survey photometry measured in the overlap region of fields 292 and 241 for the magnitude ranges (a,b) $13 < B_J < 15$; (c,d) $15 < B_J < 17$; (e,f) $17 < B_J < 19$; (g,h) $19 < B_J < 21$; and (i,j) $21 < B_J < 23$. The left-hand panels are raw differences; the right-hand panels show distributions after subtraction of positionally dependent systematic errors.

Range	N	σ_{RAW}	Stars			N	σ_{RAW}	Galaxies		
			ZP	$\sigma_{\text{-ZP}}$	σ_{REL}			ZP	$\sigma_{\text{-ZP}}$	σ_{REL}
9.0 < B _J < 10.0	51	0.55	-0.53	0.13	—	—	—	—	—	—
10.0 < B _J < 11.0	92	0.52	-0.49	0.10	—	—	—	—	—	—
11.0 < B _J < 12.0	197	0.40	-0.38	0.09	—	—	—	—	—	—
12.0 < B _J < 13.0	438	0.36	-0.35	0.11	0.03	—	—	—	—	—
13.0 < B _J < 14.0	789	0.37	-0.36	0.13	0.03	—	—	—	—	—
14.0 < B _J < 15.0	1384	0.43	-0.41	0.13	0.03	—	—	—	—	—
15.0 < B _J < 16.0	2014	0.47	-0.45	0.14	0.04	16	0.40	0.38	0.12	—
16.0 < B _J < 17.0	3105	0.46	-0.44	0.14	0.04	115	0.37	0.35	0.06	—
17.0 < B _J < 18.0	4305	0.42	-0.40	0.14	0.05	505	0.27	0.24	0.08	0.08
18.0 < B _J < 19.0	5595	0.34	-0.32	0.12	0.05	1522	0.19	0.16	0.07	0.06
19.0 < B _J < 20.0	7831	0.25	-0.23	0.12	0.06	4106	0.12	0.09	0.07	0.06
20.0 < B _J < 21.0	10851	0.17	-0.14	0.12	0.07	9509	0.10	0.01	0.10	0.09
21.0 < B _J < 22.0	18679	0.16	-0.07	0.15	0.12	13563	0.17	0.05	0.17	0.16
22.0 < B _J < 23.0	27806	0.20	-0.03	0.20	0.18	6429	0.27	0.08	0.27	0.25

Table 5. Internal systematic and random errors measured from the overlapping plate pair SERC–J fields 292 and 241.

Range	N	σ_{RAW}	Stars			N	σ_{RAW}	Galaxies		
			ZP	$\sigma_{\text{-ZP}}$	σ_{REL}			ZP	$\sigma_{\text{-ZP}}$	σ_{REL}
9.0 < R < 10.0	89	0.56	0.54	0.06	—	—	—	—	—	—
10.0 < R < 11.0	140	0.45	0.43	0.05	—	—	—	—	—	—
11.0 < R < 12.0	346	0.35	0.34	0.05	0.04	—	—	—	—	—
12.0 < R < 13.0	680	0.33	0.31	0.06	0.02	—	—	—	—	—
13.0 < R < 14.0	1281	0.29	0.28	0.07	0.03	—	—	—	—	—
14.0 < R < 15.0	2182	0.26	0.25	0.07	0.03	32	0.09	-0.09	0.04	—
15.0 < R < 16.0	3423	0.22	0.21	0.08	0.04	197	0.06	-0.05	0.04	0.03
16.0 < R < 17.0	5171	0.18	0.17	0.08	0.04	737	0.05	-0.02	0.04	0.03
17.0 < R < 18.0	7402	0.14	0.13	0.08	0.05	2556	0.05	-0.01	0.05	0.04
18.0 < R < 19.0	11035	0.11	0.09	0.09	0.06	7415	0.07	0.00	0.07	0.07
19.0 < R < 20.0	19759	0.13	0.02	0.12	0.11	11490	0.14	0.02	0.14	0.13
20.0 < R < 21.0	26514	0.18	0.07	0.17	0.16	7061	0.26	0.11	0.25	0.24

Table 6. Internal systematic and random errors measured from the overlapping plate pair AAO–R fields 292 and 241.

the magnitude range $16 < B_J < 17$. Once again, because we have calibrated out the systematic errors in colour as a function of position and magnitude, and also set the colour zero-point in every field (see Section 2.3.4) the colours are consistent at a level dictated by random errors alone. The RMS values about the $y = x$ lines in Figure 14 are ~ 0.1 mag, indicating single measurement random errors in the colours at the level of ~ 0.07 mag in this magnitude range. While this is strictly speaking a test of internal consistency, it also illustrates the true external errors in the colours (cf. Section 3.2.3) owing to the way in which any systematic errors have been eliminated.

3.2 External tests of accuracy and reliability

3.2.1 Image classification and completeness

We have assessed the accuracy of image classification and detection completeness of SGC data using 4m prime focus data from Carter (1980) and CCD data from Metcalfe et al. (1991 – hereafter MSFJ91). Those data are demonstrably deeper than that from the Schmidt plates and although they are only slightly better in terms of angular resolution (e.g. 1.5 arcsec for the MSFJ91 CCD images as opposed to ~ 2 arcsec for the SGC data) their higher signal-

to-noise ratio at a given magnitude allows thresholding at lower isophotes and therefore more reliable image classification. In Table 9 we give figures for comparison against the galaxy sample of Carter (1980). This comparison shows completeness levels of 100% down to $B_J \sim 21$ with $> 90\%$ reliability of correct classification down to $B_J \sim 20$. This is in good agreement with other estimates of the reliability of Schmidt survey galaxy catalogues (e.g. Caretta, Maia & Willmer 2000). Tables 10 and 11 give similar figures for comparison of sets of stars and galaxies from MSFJ91 against SGC J and R data. Field numbers 823 to 826 and 891, 893 and 894 were used in these comparisons (fields 4, 13, 10, 14, 2, 3 and 9 respectively in Table 1 of MSFJ91).

The reliability figures in Tables 9 and 10 clearly do not agree with the internally assessed classification accuracy estimates displayed in Figures 12(a) and (b). The reason for this is that fainter than $m \sim 20$, the typical size of detectable galaxian images is comparable to the seeing on the photographic plate material, and the image classification scheme inevitably classifies unresolved sources as stars. In Figures 12(a) to (b) the accuracy of the classification is overestimated since there is a systematic trend for objects to be classed as stellar regardless of their actual type. The false level of agreement on stellar classification potentially

Range	N	σ_{RAW}	Stars			N	σ_{RAW}	Galaxies		
			ZP	$\sigma_{\text{-ZP}}$	σ_{REL}			ZP	$\sigma_{\text{-ZP}}$	σ_{REL}
9 < I < 10	99	0.16	-0.14	0.10	—	—	—	—	—	—
10 < I < 11	217	0.36	-0.34	0.08	—	—	—	—	—	—
11 < I < 12	501	0.41	-0.39	0.07	0.04	—	—	—	—	—
12 < I < 13	1079	0.36	-0.35	0.08	0.04	—	—	—	—	—
13 < I < 14	1994	0.29	-0.28	0.07	0.04	13	0.29	0.27	0.10	—
14 < I < 15	3504	0.21	-0.20	0.07	0.04	132	0.19	0.17	0.13	—
15 < I < 16	5751	0.16	-0.15	0.07	0.05	530	0.14	0.12	0.09	0.06
16 < I < 17	7827	0.11	-0.09	0.08	0.06	2006	0.11	0.07	0.09	0.08
17 < I < 18	10050	0.11	-0.01	0.11	0.09	6195	0.14	-0.03	0.14	0.14
18 < I < 19	11213	0.17	0.01	0.17	0.16	5143	0.23	0.04	0.23	0.22

Table 7. Internal systematic and random errors measured from the overlapping plate pair SERC-I fields 292 and 241.

Range	N	σ_{RAW}	Stars			N	σ_{RAW}	Galaxies		
			ZP	$\sigma_{\text{-ZP}}$	σ_{REL}			ZP	$\sigma_{\text{-ZP}}$	σ_{REL}
9 < R < 10	65	0.06	-0.01	0.06	—	—	—	—	—	—
10 < R < 11	160	0.08	-0.07	0.07	0.05	—	—	—	—	—
11 < R < 12	340	0.16	-0.15	0.07	0.06	—	—	—	—	—
12 < R < 13	621	0.22	-0.21	0.08	0.03	—	—	—	—	—
13 < R < 14	983	0.25	-0.24	0.09	0.04	—	—	—	—	—
14 < R < 15	1461	0.23	-0.22	0.10	0.04	35	0.05	-0.02	0.05	0.05
15 < R < 16	2276	0.18	-0.17	0.10	0.05	174	0.12	-0.10	0.09	0.07
16 < R < 17	3630	0.14	-0.13	0.10	0.05	502	0.09	-0.06	0.08	0.04
17 < R < 18	5041	0.13	-0.11	0.10	0.06	1384	0.09	-0.05	0.09	0.06
18 < R < 19	6225	0.13	-0.09	0.12	0.08	3766	0.15	-0.08	0.15	0.11
19 < R < 20	8576	0.19	-0.08	0.18	0.15	5445	0.22	-0.08	0.22	0.19
20 < R < 21	4408	0.19	0.09	0.18	0.17	1379	0.30	0.24	0.25	0.22

Table 8. Internal systematic and random errors measured from the overlapping plate pair ESO-R fields 292 and 241.

leads to a correspondingly false estimate of the underlying classification accuracy for both image types; however it is clear from the internal reliability that some very faint, non-stellar sources must be consistently classified as such when it is possible to detect their non-stellar nature from the photographic data.

It is interesting to note that the reliability estimates from Table 9 were made from a field which presents a small zenith distance at the UK Schmidt Telescope, while Tables 10 and 11 are based on data at the celestial equator. This probably accounts for their poorer image classification reliability.

3.2.2 Systematic photometric errors as a function of magnitude

As illustrated in Figure 13, while the survey field photometric zeropoints are defined globally using faint objects in overlap regions along with a network of CCD standards, at increasingly bright magnitudes systematic errors become apparent. This is due to the assumption of a single global gradient for the characteristic curve for the plates in any given colour. Furthermore, it is to be expected that systematic errors will be dependent on plate position as well as magnitude, since the photographic response will not be perfectly uniform within a single plate. This is illustrated in more detail in Figure 15(a) to (d), where we have compared SGC R photometry against the SDSS calibration region A (Stone,

Pier & Monet 1999). These data are in a slightly different passband (SLOAN r as oppose to R_{59F}) but the difference is negligible at the accuracy we require, and the random errors on the CCD data are negligible compared to the photographic errors. The CCD data encompass $\sim 3.5^\circ \times 7.5^\circ$ and are therefore ideal for showing position dependent systematics over areas that traverse photographic plate boundaries.

In Figure 15(a) to (d) we have divided the data in $10 < R < 18$ into four 2 mag ranges; the vertical error vectors are scaled such that $1^m \equiv 1^\circ$. Only stars have been used in this analysis. The following points should be noted:

- In the faintest magnitude range ($R > 16$) there are no significant zeropoint errors within a field or in traversing to an adjacent field.
- There are global systematic zeropoint errors within individual fields at the level of several tenths of a magnitude for $R < 16$; these are, in general, different for different fields.
- At bright magnitudes, the systematic errors change within a single field as a function of plate position. These variations are once more at the level of several tenths of a magnitude.

3.2.3 Effective external errors in photometry

Finally, we have checked the external errors (i.e. those resulting in a straightforward comparison between an external

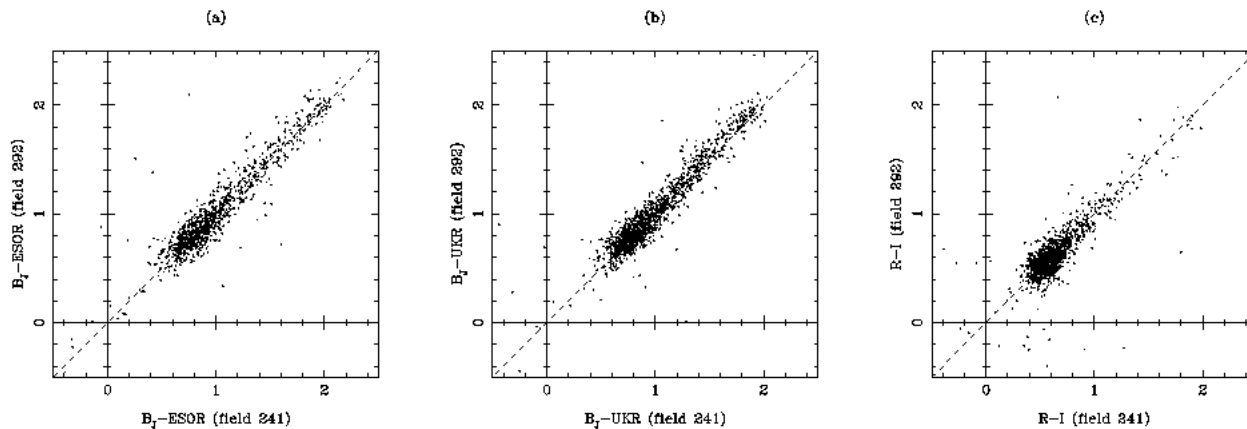


Figure 14. Comparisons of survey colours in the overlap region of fields 241 and 292 in the magnitude range $16 < B_J < 17$: (a) $B_J - R$ (ESO-R); (b) $B_J - R$ (UKR) and (c) $R - I$. The dashed lines shows $y = x$. The RMS dispersion is ~ 0.1 mag indicating single-measurement errors of ~ 0.07 mag in any colour in this magnitude range.

Magnitude range	No. of gals in Carter (1980)	No. of objects found in SGC	No. classed as galaxies	No. classed as stellar	Completeness %	Reliability %
$16.5 < B_J < 17.5$	3	3	3	0	100.0	100.0
$17.5 < B_J < 18.5$	28	28	28	0	100.0	100.0
$18.5 < B_J < 19.5$	92	91	91	0	98.9	100.0
$19.5 < B_J < 20.5$	180	174	160	14	96.7	92.0
$20.5 < B_J < 21.5$	307	302	227	75	98.4	75.2
$21.5 < B_J < 22.5$	584	515	253	262	88.2	49.1
$22.5 < B_J < 23.5$	350	149	57	92	42.6	38.3

Table 9. Comparison of the galaxy sample of Carter (1980) against the corresponding SGC J data.

dataset and our survey data, with no regard as to the systematic nature of those errors) of our BRI photometry in the equatorial zone by combining data from Landolt (1992) and Boyle et al. (1995). Note that although the Boyle et al. data have been used to measure gradients and tie down zeropoints (Sections 2.3.1 and 2.3.3), they have not been used to derive detailed individual calibration curves on a plate-by-plate basis. Galaxy photometric precision has been assessed using the Metcalfe et al. (1991) data along with data from Cunow et al. (1997 and references therein). Table 12 shows the results. The main point to note from this comparison is that brighter than $m \sim 15$, there can be large errors in the photometry (their origin is discussed previously). Fainter than this, in general the stellar photometry is typically accurate to $\sigma \sim 0.3$ (at best, $\sigma \sim 0.1$) until the respective plate limits are approached, whereupon emulsion noise begins to dominate and the random errors rise again (this is particularly noticeable for the lower s/n SERC-I and POSS-E plates). It is also clear that galaxy photometry is, in general, less accurate than stellar photometry in a given magnitude range as expected.

Figure 16 illustrates external checks on the colour indices $B_J - R$ and $B_J - I$ from the same data, in the natural systems of the photographic emulsion/filter passbands. These indicate the external accuracy of the SSS colours. Despite the presence of large systematic errors on individual magnitudes, the colours are accurate to the levels indicated in the previous internal consistency check: at $B_J \sim 16.5$, the colours are accurate to the level $\sigma_{B-R, R-I} \sim 0.07$; at

$B_J \sim 20.0$ (typical of the external comparison stars in Figure 16) the errors rise to $\sigma_{B-R, R-I} \sim 0.16$. Moreover, there is no evidence of any systematic errors in the colours greater than ~ 0.1 mag, vindicating the choice of colour zeropoints given in Table 4.

4 CONCLUSION

We have presented a detailed description of the image detection, parameterisation, classification and photometric properties of the SuperCOSMOS Sky Survey^{*}. With reference to examples from the first release of data, the South Galactic Cap (SGC) survey, we have demonstrated the typical completeness, classification reliability and photometric errors (both random and systematic). For a summary of these results along with similar comparisons for other large-scale survey programmes and a guide to using the SSS database, the reader is referred to Paper I.

ACKNOWLEDGEMENTS

The SuperCOSMOS pixel analysis software is based on original code written by Steven Beard for the predecessor machine, COSMOS. We are also grateful to Dennis Kelly for the

^{*} database available online at <http://www-wfau.roe.ac.uk/sss>

Magnitude range	Tot.	SGC	Stars				Galaxies					
			Stars	Gals	%Comp.	%Rel.	Tot.	SGC	Gals	Stars	%Comp.	%Rel.
16.5 < B _J < 17.5	8	8	8	0	100	100	—	—	—	—	—	—
17.5 < B _J < 18.5	7	7	7	0	100	100	3	3	3	0	100	100
18.5 < B _J < 19.5	12	11	11	0	92	100	4	4	4	0	100	100
19.5 < B _J < 20.5	20	19	19	0	95	100	14	14	12	2	100	86
20.5 < B _J < 21.5	42	22	18	4	52	82	53	53	33	20	100	62
21.5 < B _J < 22.5	117	34	31	3	29	91	129	76	25	51	59	33
22.5 < B _J < 23.5	174	2	2	0	1	100	363	17	7	10	5	41

Table 10. Comparison of the star/galaxy samples from Metcalfe et al. (1991) against the corresponding SGC J data.

Magnitude range	Tot.	SGC	Stars				Galaxies					
			Stars	Gals	%Comp.	%Rel.	Tot.	SGC	Gals	Stars	%Comp.	%Rel.
16.5 < R < 17.5	3	3	3	0	100	100	8	8	7	1	100	88
17.5 < R < 18.5	11	11	10	1	100	91	20	20	18	2	100	90
18.5 < R < 19.5	31	31	12	19	100	39	25	24	21	3	96	88
19.5 < R < 20.5	94	80	27	53	85	34	25	23	18	5	92	78
20.5 < R < 21.5	189	26	11	15	14	42	31	6	4	2	19	67

Table 11. Comparison of the star/galaxy samples from Metcalfe et al. (1991) against the SGC R data.

huge coding effort in writing new routines and importing existing software into the SuperCOSMOS suite. NCH is grateful to Simon Driver for discussion concerning galaxy magnitudes, to Lance Miller for his computer codes for colour corrections and to Sue Tritton and Mike Read for information concerning the various Schmidt survey plate collections. We thank Nigel Metcalfe and David Carter for supplying object catalogues from deep CCD and 4m photographic data in machine-readable form. Funding for the University of Edinburgh Institute for Astronomy Wide-Field Astronomy Unit and Institute of Astronomy Cambridge Astronomical Survey Unit is provided by the UK PPARC. This research has made use of data archived at the CDS, Strasbourg. We are indebted to the referee, Sean Urban, for a prompt and thorough review of these manuscripts.

The National Geographic Society–Palomar Observatory Sky Survey (POSS-I) was made by the California Institute of Technology with grants from the National Geographic Society. The UK Schmidt Telescope was operated by the Royal Observatory Edinburgh, with funding from the UK Science and Engineering Research Council (later the UK Particle Physics and Astronomy Research Council), until 1988 June, and thereafter by the Anglo–Australian Observatory. The blue plates of the Southern Sky Atlas and its equatorial extension (together known as the SERC–J/EJ) as well as the Equatorial Red (ER), the second epoch (red) Survey (SES or AAO–R) and the infrared (SERC–I) Survey were taken with the UK Schmidt Telescope. All data retrieved from the URLs described herein are subject to the copyright given in this copyright summary. Copyright information specific to individual plates is provided in the downloaded FITS headers.

REFERENCES

- Beard S.M., MacGillivray H.T., Thanisch P.F., 1990, *MNRAS*, 247, 311
- Bessell M.S., 1986, *PASP*, 98, 1303
- Blair M., Gilmore G., 1982, *PASP*, 94, 742
- Boyle B.J., Shanks T., Croom S.M., 1995, *MNRAS*, 276, 33
- Brownrigg D.R.K., 1984, *Communications of the A.C.M.*, 27, 807
- Bunclark P.S., Irwin M.J., 1983, in Rolfe E.J., ed., *ESA SP–201*, Proc. Symp. on Statistical Methods in Astronomy. ESA Scientific and Technical Publications Branch, Noordwijk, p. 195
- Caretta C.A., Maia M.A.G., Willmer C.N.A., 2000, *AJ*, 119, 524
- Carter D., 1980, *MNRAS*, 190, 307
- Croom S.M., Ratcliffe A., Parker Q.A., Shanks T., Boyle B.J., Smith R.J., 1999, *MNRAS*, 306, 592
- Cunow B., Duemmler R., Spiekermann G., Ungruhe R., Wargau W.F., 1997, *A&AS*, 125, 71
- Draper P.W., Eaton, N., 1999, *Starlink User Note No. 109.10*, PISA – Position, Intensity and Shape Analysis. CCLRC/Rutherford Appleton Laboratory, PPARC
- ESA, 1997, *ESA SP–1200*, The Hipparcos and Tycho Catalogues. ESA, Noordwijk
- Evans D.W., 1989, *A&AS*, 78, 249
- Goldschmidt P., Miller L., 1998, *MNRAS*, 293, 107
- Hambly N.C., Steele I.A., Hawkins M.R.S., Jameson R.F., 1995, *A&AS*, 109, 29
- Hambly N.C., Miller L., MacGillivray H.T., Herd J.T., Cormack W.A., 1998, *MNRAS*, 298, 897
- Hambly N.C. et al., 2001a, *MNRAS*, submitted (Paper I)
- Hambly N.C., Irwin M.J., Davenhall A.C., MacGillivray H.T., 2001b, *MNRAS*, submitted (Paper III)
- Heydon–Dumbleton N.H., Collins C.A., MacGillivray H.T., 1989, *MNRAS*, 238, 379
- Hoaglin, D.C., Mosteller, F., Tukey, J.W., 1983, *Understanding Robust and Exploratory Data Analysis*, Wiley, Chapter 11
- Irwin M.J., 1985, *MNRAS*, 214, 575
- Irwin M.J., McMahon R., 1992, in: *IAU Working Group on Wide-Field Imaging Newsletter No. 2*, ed. H.T. MacGillivray, p. 31
- Landolt A.U., 1992, *AJ*, 104, 340
- Lasker B.M., et al., 1988, *ApJS*, 68, 1
- MacGillivray H.T., Stobie R.S., 1984, *Vistas in Astronomy*, 27,

	SERC-EJ				SERC-ER				SERC-I				POSS-E			
	N _S	σ	N _G	σ	N _S	σ	N _G	σ	N _S	σ	N _G	σ	N _S	σ	N _G	σ
10 < m < 11	—	—	—	—	—	—	—	—	5	0.97	—	—	4	0.77	—	—
11 < m < 12	—	—	—	—	5	0.66	—	—	11	0.37	—	—	17	0.96	—	—
12 < m < 13	—	—	—	—	7	0.69	—	—	7	1.01	—	—	9	1.13	—	—
13 < m < 14	5	0.33	—	—	4	0.66	—	—	9	0.93	—	—	7	1.11	—	—
14 < m < 15	5	0.38	—	—	6	0.54	—	—	7	0.72	—	—	11	0.85	—	—
15 < m < 16	10	0.33	—	—	6	0.40	—	—	27	0.21	—	—	7	0.73	—	—
16 < m < 17	25	0.22	—	—	38	0.15	5	0.73	44	0.10	6	0.29	62	0.16	6	0.76
17 < m < 18	47	0.14	—	—	64	0.08	19	0.16	70	0.09	39	0.19	92	0.17	25	0.27
18 < m < 19	75	0.10	19	0.85	96	0.07	56	0.16	74	0.17	46	0.37	148	0.22	78	0.24
19 < m < 20	90	0.09	46	0.37	129	0.12	61	0.14	15	0.84	7	0.62	162	0.29	91	0.35
20 < m < 21	160	0.11	85	0.25	50	0.25	15	0.31	—	—	—	—	39	1.31	20	1.40
21 < m < 22	239	0.23	51	0.21	—	—	—	—	—	—	—	—	—	—	—	—
22 < m < 23	27	0.22	3	0.22	—	—	—	—	—	—	—	—	—	—	—	—

Table 12. Global external photometric accuracy of SGC data as a function of magnitude in the equatorial region for stars and galaxies (N_S and N_G respectively).

433

Maddox S.J., Efstathiou G., Sutherland W.J., 1990, MNRAS, 246, 433
 Metcalfe N., Shanks T., Fong R., Jones L.R., 1991, MNRAS, 249, 498 (MSFJ91)
 Morgan D.H., Tritton S.B., Savage A., Hartley M., Cannon R.D., 1992, in MacGillivray H.T., Thomson E.B., eds, Digitised Optical Sky Surveys. Kluwer, Dordrecht, p. 11
 Nichol B.C., 1993, PhD Thesis, Univ. Edinburgh
 Postman M., Bucciarelli B., Sturch C., Borgman T., Casalegno R., Doggett J., Costa E., 1997, in McLean B.J., Golombek D.A., Hayes J.J.E., Payne H.E., eds, Proc. IAU Symp. 179, New Horizons from Multi-wavelength Sky Surveys. Kluwer, Dordrecht, p. 379
 Stobie R.S., Sagar R., Gilmore G., 1985, A&AS, 60, 503
 Stobie R.S., 1986, Pattern Recognition Letters, 4, 317
 Stone R.C., Pier J.R., Monet D.G., 1999, AJ, 118, 2488
 Tritton S.B., 1983, UKSTU Handbook. ROE, Edinburgh
 Young C.K., Metcalfe N., Zhu J., Wu H., Chen J.-S., 1998, A&AS, 130, 173

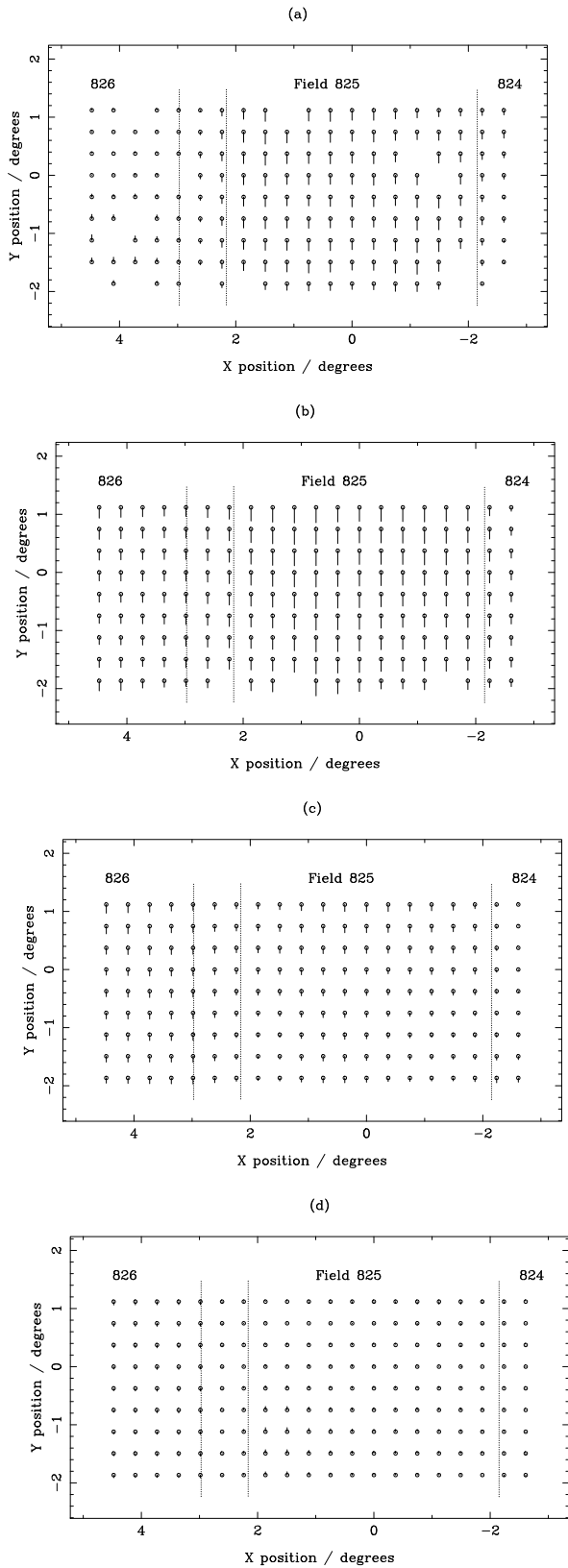


Figure 15. Positional dependent systematic errors between SGC R data and the CCD photometry of Stone et al. (1999) in SDSS calibration region ‘A’. Data are binned in ~ 2 cm bins and smoothed to show the global trends in the systematics; in plots (a) to (d) we show four 2.0 mag ranges between $10 < R < 18$. The vertical bars are scaled such that $1^\circ \equiv 1$ mag.

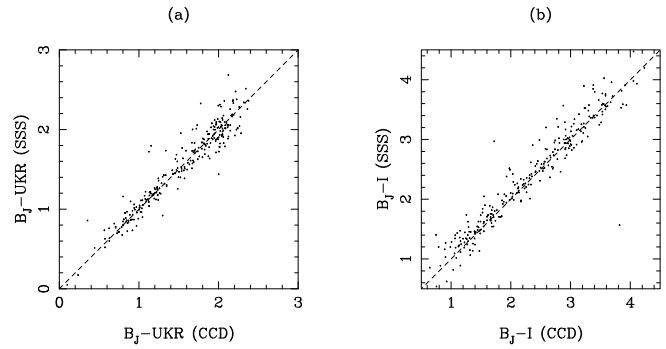


Figure 16. Comparisons of survey colours with those from Boyle et al. (1995): (a) $B_J - R$; (b) $B_J - I$. The dashed lines shows $y = x$. The RMS dispersion is ~ 0.16 mag indicating the single-measurement errors in any colour at these magnitudes (typically $B_J \sim 20$).